The Astrophysical Journal, 569:911–940, 2002 April 20

EVOLUTION, STRUCTURE, AND SEISMOLOGY OF INTERMEDIATE-MASS STARS

D. B. Guenther
Department of Astronomy and Physics, Saint Mary's University, Halifax, NS B3H 3C3, Canada;
guenther@ap.stmarys.ca
Received 2001 August 13; accepted 2001 December 21

ABSTRACT

The interior structure, the evolution, and the *p*-mode oscillation spectra of stellar models between 2.0 and 5 $M_\odot$ are presented. Interior details, including convective core and envelope growth and decay, the development of composition gradients, and the onset of hydrogen shell burning are shown to be testable by future asteroseismology observations. The stellar age and mass dependence of the large- and small-spacing oscillation frequencies are discussed. The dependencies of the structure and the oscillation spectra on composition and mixing length are also discussed. A new oscillation diagnostic for stellar mass is introduced.

Subject headings: stars: evolution — stars: interiors — stars: oscillations

1. INTRODUCTION

Numerical modeling of the equations of stellar structure and evolution, with the aid of sophisticated compilations of relevant opacities, the equation of state, and nuclear reaction rates, has successfully mapped out our understanding of the evolution of stars throughout the H-R diagram. Confirmation of stellar evolution theory has come from the wonderful agreement between the predicted positions of stars in the H-R diagram and their observed positions, and the association of different phases of evolution with specific regions in the H-R diagram. The pulsation behavior of Cepheids and other nonlinear, radially oscillating stars has further confirmed stellar modeling for specific stars. Detailed confirmation of some of the physics of the stellar model has also come from the better than one part in one thousand agreement between the oscillation spectrum predicted by the standard solar model and the observed solar *p*-mode oscillation spectrum. Additionally, and recently, is the conclusion from the Sudbury Solar Neutrino Observatory (SNO) collaboration (Ahmad, Allen, & Andersen 2001), using SNO (Boger et al. 2000) and Super-Kamiokande (Fukuda et al. 1998) data, that the electron neutrino has mass and hence oscillates, thus confirming that the nuclear physics of the solar model is correct, that is, specifically, that both the *p*-*p* and CNO chains contribute to the solar luminosity.

There remain many aspects of stellar theory that have not been observationally confirmed. The matching of theoretical and observational H-R diagrams does not unambiguously confirm the interior structure predictions of the stellar models. With the exception of a few pulsating stars, our picture of the stellar interior is derived exclusively from the physics of the stellar model, constrained by the observed surface boundary conditions. Although it is unlikely that the basic physics is in error, the opacities, the equation of state, the model of convection, and the atmosphere calculation are uncertain to varying degrees. The uncertainties in the opacity and equation-of-state calculations are estimated to be approximately $\pm 15\%$ for conditions that exist in the deep interior of stars and as much as $\pm 30\%$ in the cooler outer layers. The mixing-length approximation, which has long been suspect, is now known to incorrectly specify the structure of the surface layers in the Sun, as demonstrated from seismic studies of the *p*-mode oscillation spectrum (Demarque, Guenther, & Kim 1999). Furthermore, the physics of the stellar model does not include the effects of rotation or magnetic fields, which may turn out to be important.

As is often stated, *p*-mode oscillation data from stars will help constrain and test stellar models. Initially, oscillation data will be used to constrain the models, for example, by providing a determination of the radii of stars. Ultimately, the data will be used to test stellar interiors and evolution.

Under the unrealistically ideal situation where the observational data are well determined, one can approach the problem of how to use the oscillation data by comparing the number of constraints to the number of variables in the problem. Consider first a single star. To model an isolated star, we need to know the mass, M, age, a, luminosity, L, surface temperature, $T_{\rm eff}$, helium abundance, Y, heavy element abundance, Z, and mixing-length parameter, α. In order to obtain the luminosity of a star, we must know its distance and bolometric magnitude. The latter can be obtained by applying a bolometric correction, which depends on surface temperature and mass, to the apparent magnitude. In total, there are eight independent parameters. In the case of the Sun, we know well six of the eight constraints directly, the mass, age, bolometric flux from the Sun at the Earth, surface temperature, heavy-element abundance, and distance. The theory of stellar evolution provides two additional constraints, $L(M, a, Y, Z, \alpha)$ and $T_{\rm eff}(M, a, Y, Z, \alpha)$, which are all that are required to uniquely specify the system. Indeed, the most accurate determination of the helium abundance in the interior of the Sun comes from the solar model.

Returning to the general case of a field star, two of the eight constraints come from stellar modeling, i.e., from $L(M, a, Y, Z, \alpha)$ and $T_{\rm eff}(M, a, Y, Z, \alpha)$. The metallicity can be determined from [Fe/H] measurements, the effective temperature from atmosphere models, or simply from $B-V$. The apparent magnitude of the star and its color can be used to determine the apparent bolometric magnitude of the star. If the parallax of the star is known, then two additional constraints are needed. Therefore, some assumptions must be made about the star in order to specify it uniquely.

Normally, the stellar modeler will assume values for α and Y, for example, using the same values as obtained for the standard solar model. For field stars, p-mode oscillation data, even just the large and small spacings (defined later) will be enough to fully constrain the system. Indeed, once the system is fully constrained, the stellar model immediately gives the age, the radius, the helium abundance, and the mixing-length parameter of the star.

For binary star systems, such as α Cen AB, the number of constraints required to produce unique models of both stars increases to only 12 because of the common origin of both stars. The required constraints are the masses of the two stars, the apparent bolometric magnitudes of the two stars (which with the distance gives the luminosity of the two stars), the surface temperatures of the two stars, the age of the binary system, the helium and heavy-element abundance of the system, the distance to the system, and the mixing-length parameter of each of the two stars. Stellar evolution provides four constraints: $L_{\rm A}(M_{\rm A}, a, Y, Z, \alpha_{\rm A})$, $T_{\rm A}(M_{\rm A}, a, Y, Z, \alpha_{\rm A})$, $L_{\rm B}(M_{\rm B}, a, Y, Z, \alpha_{\rm B})$, and $T_{\rm B}(M_{\rm B}, a, Y, Z, \alpha_{\rm B})$. The composition of the system, the color of each star, the apparent magnitude of each star, the orbit ephemeris, and the parallax are enough to completely constrain the system. Therefore, for binary stellar systems of known distance, oscillation data can be used to test the models, in much the same way that they have been used to test the solar model.

Real data used to constrain stellar models have associated uncertainties that must be accounted for in any stellar modeling analysis. In the case of α Cen AB, Guenther & Demarque (1997) describe in detail how current observations can be used to constrain the system to a small range of uncertainty in the physical variables. They argue that with the addition of p-mode oscillation data, the range of uncertainty in the models is further constrained and that some internal features of the stars can be tested (e.g., the core convective region).

Another aspect of stellar modeling should be noted. That the solar model is a good fit to all observables means only that the model physics works for the specific conditions in the Sun. We currently have no way of testing whether or not the detailed physics are applicable to all stars. We do not know, for example, whether our opacity calculations are accurate at lower temperatures. We do not know whether our calibration of the rate at which helium diffuses out of the convection zone base is correct for convection zones with different depths. We do not know whether the rates of nuclear burning are correct for more massive stars where the CNO cycle dominates. We do not know to what degree convective overshooting occurs. What is needed, and what stellar p-mode oscillation data potentially offer, are new constraints to test our basic models of stars of different mass, age, and composition.

Several groups are modeling three-dimensional turbulent convection in the solar regime (Nordlund & Stein 1996; Kim & Chan 1998) and have stated plans to extend their convection models to other stars. And Deupree (2001) is now calculating full two-dimensional models of the effects of rotation in the interior of star. Stellar oscillation data will be especially critical in testing these new stellar model physics.

The purpose of this paper is to explore in greater detail the potential that asteroseismology holds in testing stellar structure and evolution theory. In this paper we focus on stars with masses between 2 and 5 $M_{\odot}$.[1] We begin with a review of the basic results of stellar evolution for stars in this mass range and then follow with a discussion of the p-mode seismology of these stars. We identify basic features of the oscillation spectrum and match them with features in the interior of the stars. Finally, we show how the stellar oscillation spectrum of a star evolves as the star itself evolves.

2. STELLAR MODELS

All stellar model sequences were calculated using YREC (Guenther et al. 1992), the Yale stellar evolution code. The same code is in use by the original author of the code, P. Demarque (Yale), and his collaborators (e.g., Demarque et al. 2001). Modified versions of the code, adapted to specific problems, are in use by M. Pinsonneault (Ohio) and his collaborators (e.g., Bahcall, Pinsonneault, & Basu 2001), B. Chaboyer (Dartmouth) and his collaborators (e.g., Chaboyer, Sarajedini, & Armandroff 2000), and A. Sills (e.g., Sills et al. 2001).

The code solves the basic equations of stellar evolution using the Henyey relaxation technique. The opacities are obtained from the OPAL98 tables (Iglesias & Rogers 1996) for temperatures above 6000 K and from the Alexander & Ferguson (1994) "molecular" opacity tables below 15,000 K. A weighted average, derived from a linear ramp function in temperature, is used in the transition temperature range. The composition of heavier than helium elements for all the stellar models is determined by scaling the observed solar mixture of elements as summarized by Grevesse, Noels, & Sauval (1996). This is also the mixture on which the opacity tables are based. The current equation-of-state tables from Lawrence Livermore (Rogers 1986; Rogers, Swenson, & Iglesias 1996) are used. The nuclear energy generation routines have been updated to include the latest cross sections (Bahcall et al. 2001). The updated cross sections altered the luminosity of our stellar models by less than one part in one thousand.

The evolutionary sequences presented here begin on the zero-age main sequence (ZAMS), defined as the point in the evolution, following pre–main-sequence collapse, where the nuclear luminosity becomes important, that is, rising above 1% of the total luminosity (gravitational collapse luminosity dominates prior to the ZAMS). The ZAMS starting models themselves were obtained by evolving Lane-Emden gas spheres from the Hayashi track to the ZAMS using YREC.

In order to obtain oscillation frequencies that are numerically accurate to $\pm 0.1\%$, the models must be represented by a relatively dense grid of shells (when compared to traditional stellar models), especially in the outer envelope and atmosphere. The stellar models discussed in this paper all have approximately 2000 shells, with one-third of the shells covering the interior, one-third covering the outer envelope, which encompasses less than 1% of the total mass, and one-third covering the atmosphere. The atmosphere is a gray atmosphere in the Eddington approximation.

The mixing-length parameter, α, was obtained from a calibrated solar model that was constructed using the same

[1] Stars between 2 and 5 $M_{\odot}$ do not develop convective envelopes until they approach the giant branch and hence are not expected to have observable nonradial oscillations until then. Near the giant branch, though, one expects, based on scaling arguments (Kjeldsen & Bedding 1995) that the luminosity variations associated with p-mode oscillations may be 100–1000 times greater than in the Sun.

physics, i.e., opacities, equation of state, and atmosphere, as used in these stellar models. Convective overshoot, rotation, and gravitational settling of helium and heavier elements were not included in the models. It is possible, though, that these additional physics will produce an observable effect on the *p*-mode oscillation modes and hence are worth studying in the future.

3. TRACKS

Evolutionary tracks were constructed for models at 2.0, 2.5, 3.0, 4.0, and 5.0 $M_\odot$. The evolutionary sequences were terminated shortly after the stellar models began ascending the giant branch. The helium abundance (mass fraction) was set to $Y = 0.24$, and the heavy-element abundance was set to $Z = 0.01$ for most of the models.

To study the effect of different values of Y and Z, additional tracks were calculated for the 3.0 $M_\odot$ models at $Y = 0.25$ and 0.26 and at $Z = 0.005$ and 0.02. Another set of tracks was also calculated for the 3.0 $M_\odot$ models with the mixing-length parameter set slightly below and above its solar model–calibrated value of $\alpha = 1.6$, that is, with α at 1.4 and 1.8.

The stellar evolution code automatically adjusts the time-step size between models along an evolutionary track according to various criteria associated with the magnitude of the structural changes taking place. For example, during main-sequence evolution, the code uses the rate at which the abundance of hydrogen decreases in the core to control the time step, and then during giant branch evolution, the code uses the rate that the mass of the hydrogen-burning shell decreases to control the time step. As a consequence, the models are not regularly spaced along the track as seen in the H-R diagram, nor are they regularly spaced in time.

Each track consists of a time sequence of approximately 2500 models. Because each model contains over 2000 shells, it is not practical or necessary to examine the detailed structure and pulsation spectrum of every model calculated. To reduce the number of models to a more manageable level, approximately 300 models, equally spaced along the track (as viewed in an H-R diagram) were selected for detailed pulsation analysis. In addition, 12 models, positioned at key points along the track, were selected for detailed interior analysis. The 12 points along the track are identified in tables and figures by the following nomenclature, listed in order of increasing age: ms1 (the ZAMS model), ms2, to1 (just before core hydrogen exhaustion during the main-sequence phase), to2 (turnoff), to3, sg1 (isothermal core collapses), sg2, sg3 (rapid evolution to subgiant phase), sg4, sg5, gb1 (beginning of giant branch evolution), and gb2. In Figure 1 we show the evolutionary tracks of the models with the 12 points identified along each track. Some physical properties of the selected models are listed in Table 1.

In Figure 2*b* we show the 3 $M_\odot$ tracks for models with different metallicities Z (0.005, 0.010, and 0.020). Increasing Z causes the opacities near the surface of the cooler models (on the giant branch) to increase. This is because the metals provide electrons, owing to their low ionization temperature, to form H^-, which is the dominant opacity source at low temperatures. An increase in the opacity near the surface causes the giant branch to shift to the red, with the envelope of the model being more distended. The effect of the metals elsewhere is different. Increasing Z prior to reaching the giant branch increases the abundance of C, N, and O in the nuclear-burning core. As a consequence, the point at which CNO burning becomes a greater contributor to the total luminosity than *p*-*p* burning takes place slightly earlier in the evolution of the star. Hydrogen is exhausted in the core earlier, and turnoff occurs at lower luminosities.

In Figure 2*c* we show the 3 $M_\odot$ tracks for models with $Y = 0.24$, 0.25, and 0.26. Increasing the helium abundance increases the mean molecular weight, and as a consequence, the luminosity of the star increases.[2]

In Figure 2*d*, we show the 3 $M_\odot$ tracks for models with $\alpha = 1.4$, 1.6 (calibrated solar value), and 1.8. The effect of the mixing-length parameter on the models is minimal until the stellar model develops a convective envelope, near $\log T_{\rm eff} = 3.8$.

4. EVOLUTION OF STRUCTURE

4.1. *Age Scale*

Because the rate of evolution varies significantly from the main-sequence to the giant branch, it is necessary to adopt a nonlinear timescale. We use the total arc length, λ, measured from the ZAMS, along the model's evolutionary track in the H-R diagram to stand in for the age scale of the models. During phases of evolution when the interior structure is undergoing rapid changes, the position of the star, in the H-R diagram, changes rapidly, and during more quiescent phases of evolution, such as during main-sequence evolution, the H-R diagram position of the star does not change very much. Figure 3, which is a plot of age versus λ (the scale of which is arbitrary) for the 2–5.0 $M_\odot$ evolutionary sequences, can be used to convert between the two age scales. The 12 specifically selected models along the evolutionary sequence are identified.

4.2. *Pressure, Temperature, Density, and Luminosity*

The evolution of the interior structure of stars between 2 and 5.0 $M_\odot$ was well studied by stellar modelers in the 1960s. Iben's (1967) review article provides detailed physical explanations of the interior evolution of a 5.0 $M_\odot$ star and, indeed, summarizes most of the results that remain valid today. For comparison purposes and as a general reference, we provide detailed plots of the interior structure of the 2 and 5.0 $M_\odot$ models at the 12 selected points along the evolution (Figs. 4–11).

Qualitatively, the circa 1960s through 1980s models are very similar to present-day models. Differences lie in the details. Present-day models used in pulsation studies are constructed using approximately 10 times more shells and include significantly more detailed and up-to-date atomic and nuclear physics. These improvements have been tested and calibrated in the solar model. Consider that the theoretical oscillation spectrum of a circa 1970s standard solar model (Iben & Mahaffy 1976) did not match the observed solar oscillation spectrum to better than one part in one hundred. Today, the oscillation spectrum of the standard solar model matches the observations to better than one part in one thousand, all without any ad hoc tweaking of the physics.

[2] Chandrasekhar (1957, pp. 273-274) shows that $L \propto \mu^{7.5} M^{5.5} R^{0.5}$, assuming conservation of mass, hydrostatic equilibrium, radiative energy transport, and a Kramers's opacity law.

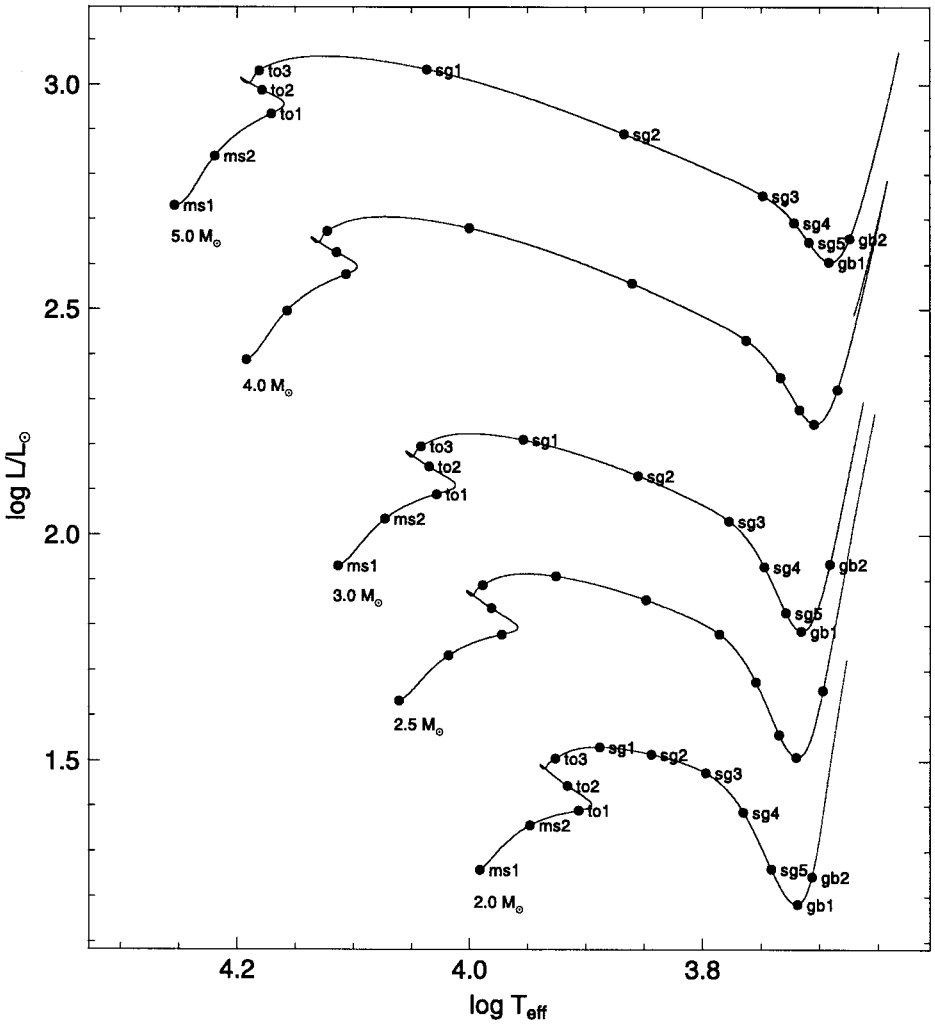

FIG. 1.—H-R diagram of stellar evolutionary tracks of stars of intermediate mass. Twelve labeled points along each track identify key phases of evolution.

Figures 4 and 5 show the run of density, ρ, at the 12 selected phases of evolution for the 2 and 5 $M_\odot$ models, respectively. Figures 6 and 7 show the run of temperature, T; Figures 8 and 9 show the run of pressure, P; and Figures 10 and 11 show the run (in the inner regions only) of luminosity, L (by convention L includes nuclear power and gravitational power but excludes neutrino power). All variables are plotted in cgs units.

The plots reveal the basic flow of stellar evolution as the core becomes more centrally concentrated and hotter and the outer envelope becomes more distended. The changes that occur in the structure of the 2 $M_\odot$ model, as the star evolves, are very similar to the changes that occur in the 5 $M_\odot$ model. During main-sequence evolution, the source of nuclear power is spread over a large region of the core (Figures 10 and 11), then as the star evolves off the main-sequence, following core hydrogen exhaustion, nuclear burning confines itself to an ever narrowing shell. With regard to pulsation, we note that by the time a star becomes a subgiant very little mass is contained within the envelope of the star.

4.3. *Convective Envelopes*

One of the more interesting features of the interior that does reveal itself in the p-mode oscillation spectrum is the presence of convective regions. Fundamentally, since we believe nonradial p-mode oscillations are driven by turbulent convection, an envelope convective region must be present in stars with observable p-mode oscillations. Needless to say, if we were to observe p-modes in stars which we predict do not have convective envelopes, then we would be forced to consider alternate driving mechanisms for the p-mode oscillations in those stars.

By simply identifying the existence or nonexistence of p-mode oscillations in a variety of stars in a cluster (i.e., a common origin group of stars), one can determine the location of the boundary between stars with and without convective envelopes. By comparing this boundary with that predicted by stellar models, we can test the basic stellar structure physics (e.g., surface boundary conditions, opacities, and equation of state) upon which the existence of a convective envelope depends. Indeed, because the position of the boundary depends on metallicity (see below), it may be possible to use the p-mode–determined position to determine, or at least confirm, the metallicity of the star cluster.

We stress that in order to carry out this seismological analysis of stellar convection, only the power envelope of the p-mode spectrum needs to be observed. The individual modes or frequency spacings do not need to be resolved. Consider, for example, the ground-based observations of

TABLE 1

SELECTED MODEL STRUCTURE PROPERTIES

Mass ($M_\odot$) (1)	Label (2)	λ (3)	Age (Gyr) (4)	$\log T_{\rm eff}$ (5)	$\log L/L_\odot$ (6)	$\log R/R_\odot$ (7)	$\log g$ (8)	$M_{\rm cc}$ (9)	$M_{\rm cenv}$ (10)	$X_{\rm cenv}$ (11)	$\log P_c$ (12)	$\log T_c$ (13)	$\log \rho_c$ (14)	X_c (15)
2.0.....	ms1	0	0.019	3.991	1.259	0.171	4.40	0.28	0.00	1.00	17.339	7.334	1.864	0.73
2.0.....	ms2	27	0.574	3.948	1.357	0.307	4.13	0.22	0.00	1.00	17.271	7.364	1.903	0.37
2.0.....	to1	39	0.784	3.906	1.391	0.407	3.92	0.16	0.00	1.00	17.282	7.400	2.001	0.13
2.0.....	to2	54	0.858	3.915	1.445	0.415	3.91	0.10	0.00	1.00	17.504	7.472	2.231	0.01
2.0.....	to3	78	0.868	3.926	1.505	0.425	3.89	0.00	0.00	1.00	18.046	7.395	2.847	0.00
2.0.....	sg1	94	0.900	3.888	1.531	0.513	3.71	0.00	0.00	1.00	18.629	7.422	3.373	0.00
2.0.....	sg2	109	0.909	3.844	1.515	0.594	3.55	0.00	0.00	1.00	19.038	7.485	3.689	0.00
2.0.....	sg3	128	0.914	3.797	1.474	0.666	3.41	0.00	0.00	1.00	19.352	7.549	3.914	0.00
2.0.....	sg4	154	0.918	3.765	1.386	0.687	3.37	0.00	0.01	0.79	19.635	7.611	4.112	0.00
2.0.....	sg5	185	0.921	3.741	1.261	0.671	3.40	0.00	0.10	0.66	19.848	7.657	4.258	0.00
2.0.....	gb1	208	0.924	3.719	1.184	0.677	3.38	0.00	0.52	0.52	20.054	7.697	4.400	0.00
2.0.....	gb2	224	0.927	3.707	1.244	0.732	3.27	0.00	1.04	0.38	20.236	7.723	4.527	0.00
2.5.....	ms1	0	0.011	4.061	1.633	0.219	4.40	0.45	0.00	1.00	17.263	7.367	1.755	0.73
2.5.....	ms2	31	0.298	4.018	1.733	0.355	4.13	0.33	0.00	1.00	17.167	7.387	1.761	0.41
2.5.....	to1	44	0.427	3.972	1.779	0.469	3.90	0.22	0.00	1.00	17.167	7.423	1.853	0.15
2.5.....	to2	60	0.471	3.981	1.837	0.480	3.87	0.13	0.00	1.00	17.407	7.502	2.103	0.01
2.5.....	to3	84	0.474	3.989	1.889	0.491	3.85	0.00	0.00	1.00	17.918	7.427	2.691	0.00
2.5.....	sg1	108	0.491	3.925	1.908	0.627	3.58	0.00	0.00	1.00	18.746	7.490	3.425	0.00
2.5.....	sg2	136	0.494	3.848	1.856	0.755	3.33	0.00	0.00	1.00	19.239	7.593	3.790	0.00
2.5.....	sg3	162	0.495	3.785	1.780	0.843	3.15	0.00	0.00	1.00	19.488	7.653	3.965	0.00
2.5.....	sg4	188	0.496	3.755	1.675	0.852	3.13	0.00	0.01	0.78	19.661	7.694	4.085	0.00
2.5.....	sg5	210	0.497	3.735	1.559	0.834	3.17	0.00	0.11	0.67	19.792	7.726	4.176	0.00
2.5.....	gb1	223	0.497	3.720	1.508	0.838	3.16	0.00	0.42	0.58	19.895	7.750	4.247	0.00
2.5.....	gb2	259	0.499	3.697	1.656	0.957	2.92	0.00	1.53	0.32	20.149	7.802	4.426	0.00
3.0.....	ms1	0	0.007	4.113	1.931	0.263	4.39	0.61	0.00	1.00	17.188	7.390	1.657	0.73
3.0.....	ms2	30	0.182	4.073	2.035	0.396	4.12	0.44	0.00	1.00	17.082	7.406	1.649	0.42
3.0.....	to1	46	0.264	4.028	2.091	0.512	3.89	0.29	0.00	1.00	17.073	7.440	1.732	0.16
3.0.....	to2	63	0.294	4.035	2.152	0.530	3.86	0.16	0.00	1.00	17.325	7.524	1.998	0.01
3.0.....	to3	86	0.295	4.042	2.197	0.538	3.84	0.00	0.00	1.00	17.800	7.456	2.547	0.00
3.0.....	sg1	119	0.305	3.954	2.211	0.722	3.47	0.00	0.00	1.00	18.848	7.555	3.466	0.00
3.0.....	sg2	156	0.307	3.855	2.132	0.880	3.16	0.00	0.00	1.00	19.341	7.672	3.823	0.00
3.0.....	sg3	187	0.307	3.777	2.031	0.985	2.95	0.00	0.00	1.00	19.558	7.727	3.975	0.00
3.0.....	sg4	210	0.308	3.747	1.929	0.994	2.93	0.00	0.01	0.79	19.676	7.757	4.058	0.00
3.0.....	sg5	226	0.308	3.729	1.828	0.979	2.96	0.00	0.11	0.69	19.772	7.781	4.124	0.00
3.0.....	gb1	236	0.308	3.716	1.787	0.985	2.94	0.00	0.38	0.60	19.845	7.800	4.175	0.00
3.0.....	gb2	261	0.308	3.692	1.936	1.108	2.70	0.00	1.54	0.38	20.032	7.843	4.306	0.00
4.0.....	ms1	0	0.004	4.192	2.389	0.334	4.37	0.92	0.00	1.00	17.061	7.421	1.497	0.73
4.0.....	ms2	28	0.085	4.157	2.496	0.458	4.12	0.65	0.00	1.00	16.950	7.434	1.474	0.45
4.0.....	to1	53	0.133	4.106	2.577	0.600	3.84	0.38	0.00	1.00	16.944	7.478	1.578	0.13
4.0.....	to2	65	0.144	4.115	2.626	0.608	3.82	0.24	0.00	1.00	17.167	7.550	1.807	0.01
4.0.....	to3	90	0.145	4.122	2.673	0.616	3.81	0.00	0.00	1.00	17.684	7.494	2.393	0.00
4.0.....	sg1	135	0.149	4.000	2.680	0.864	3.31	0.00	0.00	1.00	18.975	7.658	3.498	0.00
4.0.....	sg2	186	0.149	3.860	2.558	1.082	2.88	0.00	0.00	1.00	19.475	7.788	3.854	0.00
4.0.....	sg3	223	0.149	3.763	2.432	1.214	2.61	0.00	0.00	1.00	19.646	7.835	3.974	0.00
4.0.....	sg4	238	0.149	3.734	2.350	1.231	2.58	0.00	0.01	0.79	19.715	7.853	4.022	0.00
4.0.....	sg5	249	0.149	3.717	2.279	1.228	2.58	0.00	0.09	0.70	19.769	7.868	4.060	0.00
4.0.....	gb1	257	0.149	3.705	2.246	1.237	2.57	0.00	0.33	0.63	19.818	7.880	4.094	0.00
4.0.....	gb2	268	0.150	3.685	2.323	1.315	2.41	0.00	1.22	0.49	19.896	7.901	4.149	0.00
5.0.....	ms1	0	0.000	4.254	2.730	0.382	4.37	1.18	0.00	1.00	16.982	7.447	1.386	0.75
5.0.....	ms2	26	0.049	4.219	2.840	0.505	4.13	0.90	0.00	1.00	16.852	7.454	1.344	0.47
5.0.....	to1	55	0.079	4.170	2.935	0.651	3.84	0.53	0.00	1.00	16.842	7.499	1.444	0.14
5.0.....	to2	68	0.086	4.179	2.988	0.660	3.82	0.33	0.00	1.00	17.090	7.578	1.696	0.01
5.0.....	to3	92	0.087	4.181	3.030	0.677	3.78	0.00	0.00	1.00	17.624	7.526	2.301	0.00
5.0.....	sg1	144	0.089	4.037	3.034	0.967	3.20	0.00	0.00	1.00	19.045	7.734	3.497	0.00
5.0.....	sg2	203	0.089	3.867	2.890	1.235	2.67	0.00	0.00	1.00	19.539	7.869	3.847	0.00
5.0.....	sg3	244	0.089	3.748	2.752	1.403	2.33	0.00	0.00	1.00	19.691	7.911	3.954	0.00
5.0.....	sg4	255	0.089	3.722	2.692	1.426	2.28	0.00	0.01	0.80	19.733	7.923	3.983	0.00
5.0.....	sg5	262	0.089	3.710	2.649	1.429	2.28	0.00	0.06	0.73	19.761	7.930	4.002	0.00
5.0.....	gb1	272	0.089	3.692	2.606	1.442	2.25	0.00	0.35	0.63	19.807	7.943	4.035	0.00
5.0.....	gb2	281	0.089	3.675	2.658	1.503	2.13	0.00	1.20	0.51	19.855	7.956	4.069	0.00

NOTES.—Col. (1): Mass. Col. (2): Label of the evolutionary phase of the model. Col. (3): λ (arc length of track in H-R diagram). Col. (4): Age. Col. (5): The log of the effective temperature. Col. (6): The log of the luminosity. Col. (7): The log of the radius. Col. (9): Mass of the convective core. Col. (10): Mass of the convective envelope. Col. (11): Radius fraction location of the base of the convective envelope. Col. (12): The log of the central pressure. Col. (13): The log of the central temperature. Col. (14): The log of the central density. Col. (15): Central mass fraction abundance of hydrogen.

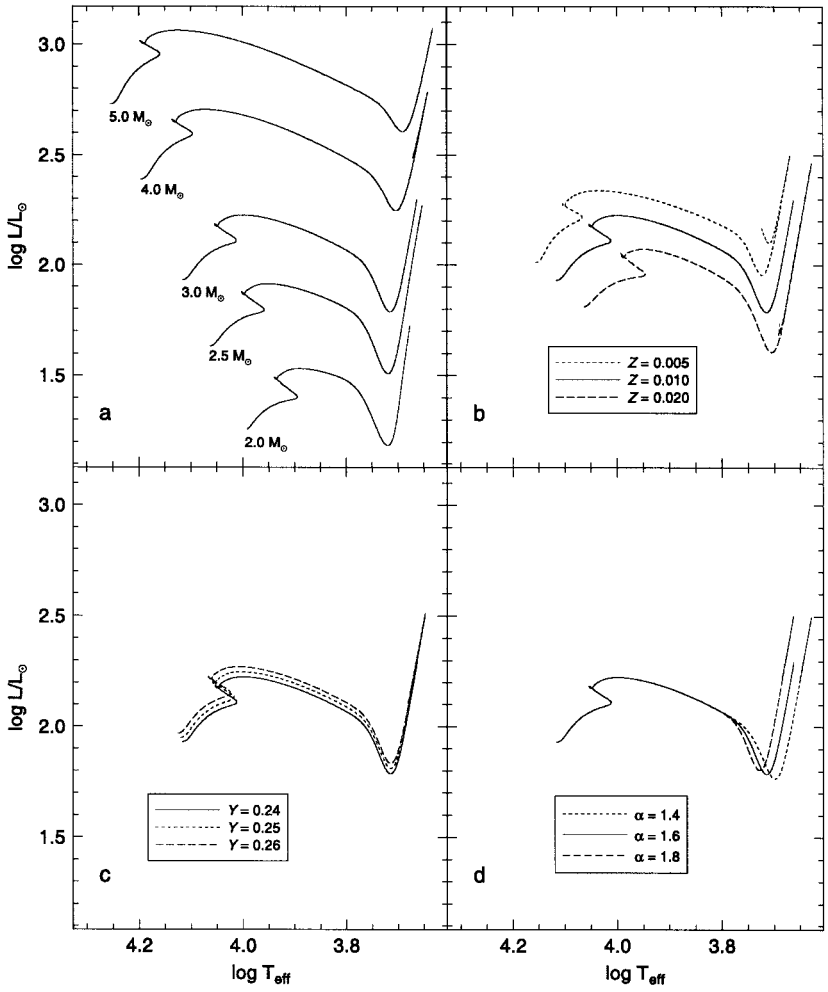

FIG. 2.—H-R diagrams of stellar evolutionary tracks show the effect of varying composition and mixing-length parameter. (*a*) All tracks for stars of intermediate mass, shown for scale and reference. (*b*) The evolutionary tracks for a 3 $M_\odot$ model with different metallicities, Z. (*c*) The evolutionary tracks for a 3 $M_\odot$ model with different helium abundances, Y. (*d*) The evolutionary tracks for a 3 $M_\odot$ model with different mixing-length parameters, α.

Procyon (Brown 1991), which do not resolve individual *p*-modes but do reveal the power envelope of the *p*-mode oscillations. The existence of the *p*-mode power spectrum implies (assuming that *p*-modes are driven exclusively by turbulent convection) that Procyon does have a convective envelope. Models of Procyon (Guenther & Demarque 1993) do have a convective envelope, a very shallow one.

In Figure 12, we plot the evolution of the convective core and convective envelope mass for the 2.0–5.0 $M_\odot$ models. Key points along the evolution are indicated by hatch marks along the top of each panel that correspond to the 12 selected models along each track. As shown, a convective envelope does not appear until the surface of the star is cool enough for the outer opacities to increase, which occurs near the subgiant phase for stars in the mass range considered here. The appearance and extent of the convective envelope depends on the heavy-element abundance (Fig. 13), which, through ionized electrons, contributes to the H^- opacity at the surface. Increasing the metal abundance increases the opacity and, in turn, forces the outer envelope to become convective earlier in the star's move toward the giant branch. In summary, the precise location on the H-R diagram of the appearance of a convective envelope as revealed by the existence of *p*-mode oscillations tests the surface physics of our stellar models.

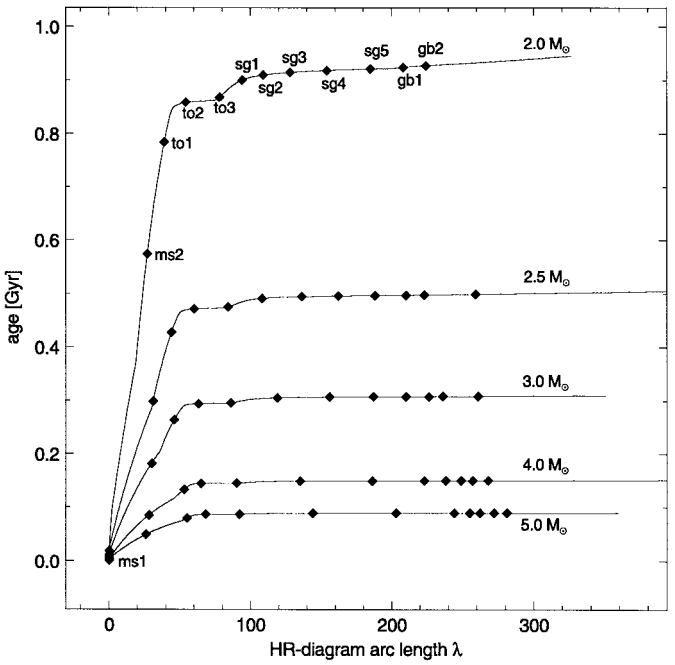

FIG. 3.—Age vs. the evolutionary track arc length, λ, as viewed in an H-R diagram. The arc length provides a more useful timescale in which to represent the structural changes that occur in stars during their evolution. Twelve points along each curve identify key phases of evolution.

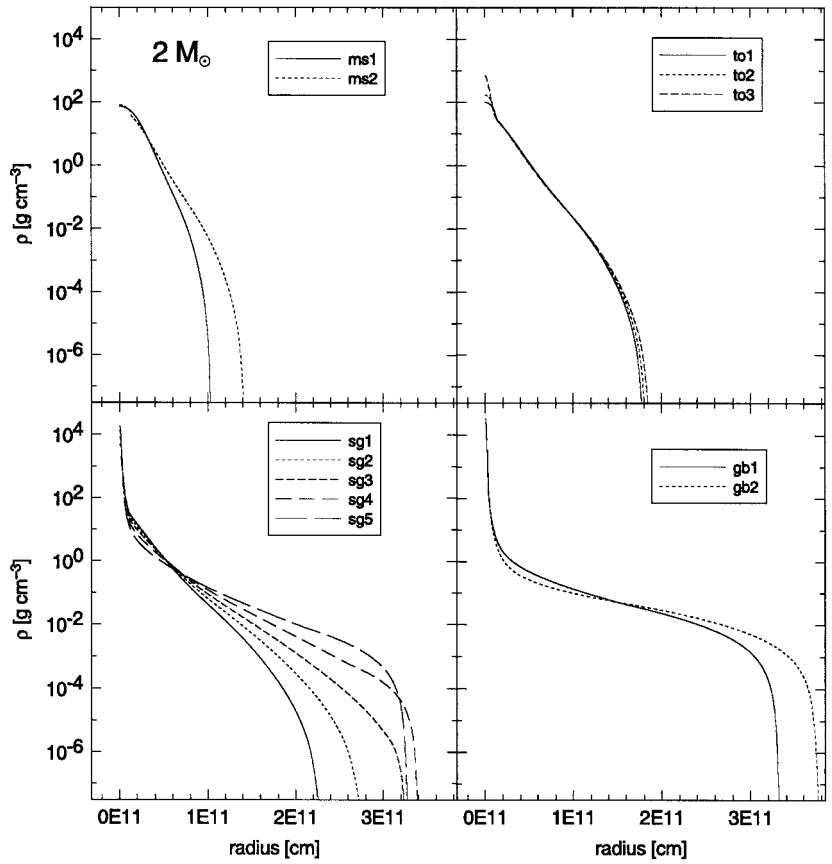

FIG. 4.—Density, ρ, vs. radius for the 2 $M_{\odot}$ models at 12 selected points (see Fig. 1) along the evolutionary track of the star

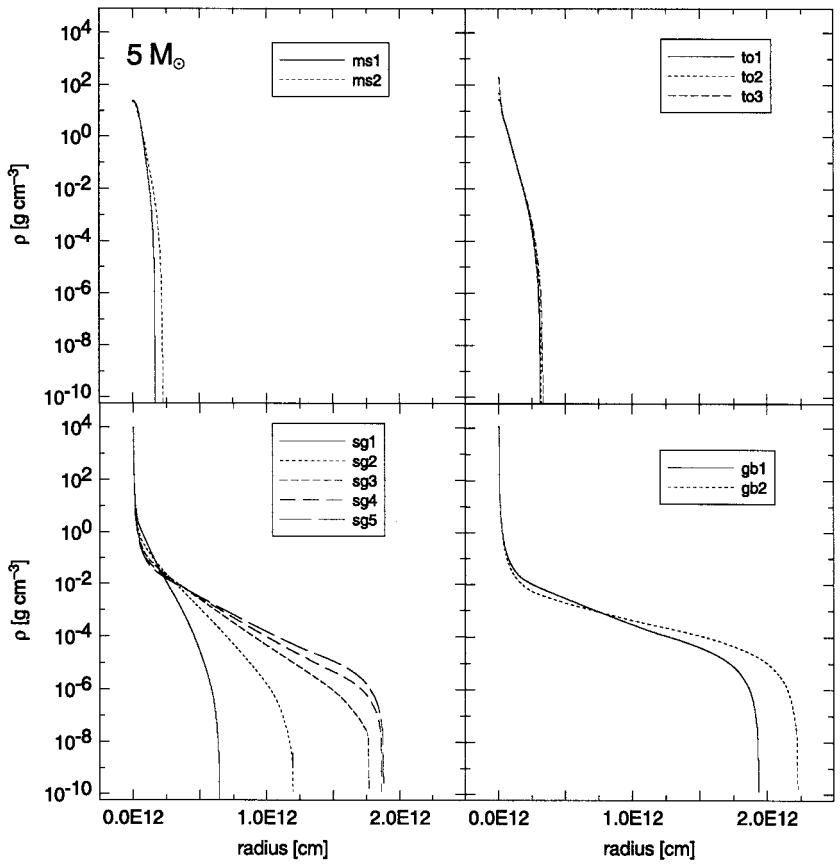

FIG. 5.—Density, ρ, vs. radius for the 5 $M_{\odot}$ models at 12 selected points along the evolutionary track of the star

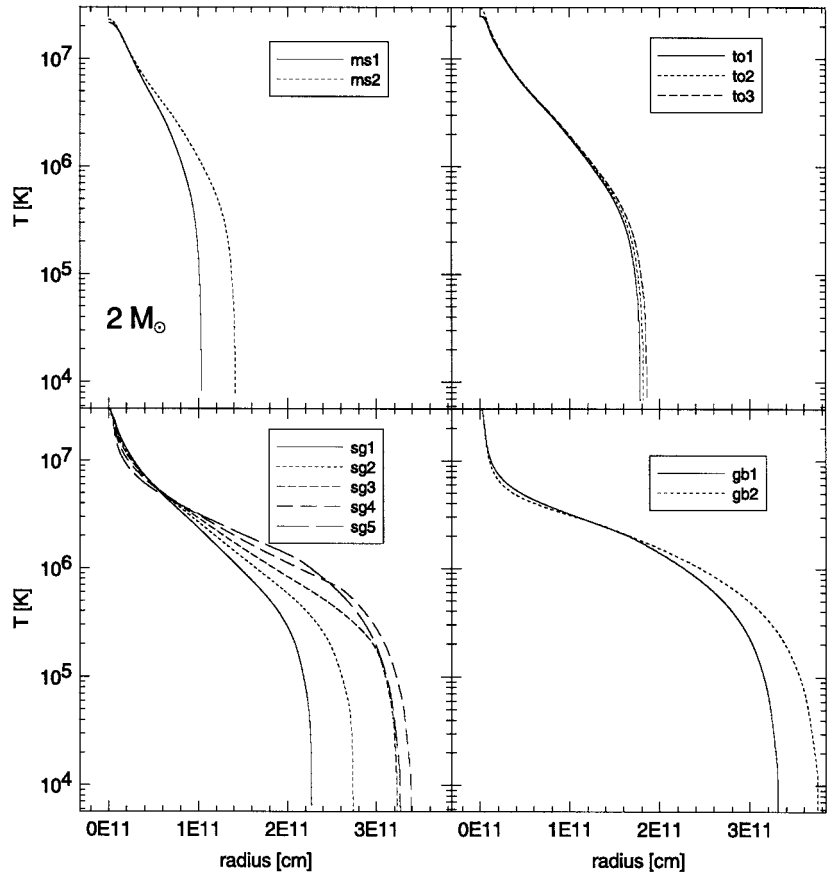

FIG. 6.—Temperature, T, vs. radius for the 2 $M_{\odot}$ models at 12 selected points along the evolutionary track of the star

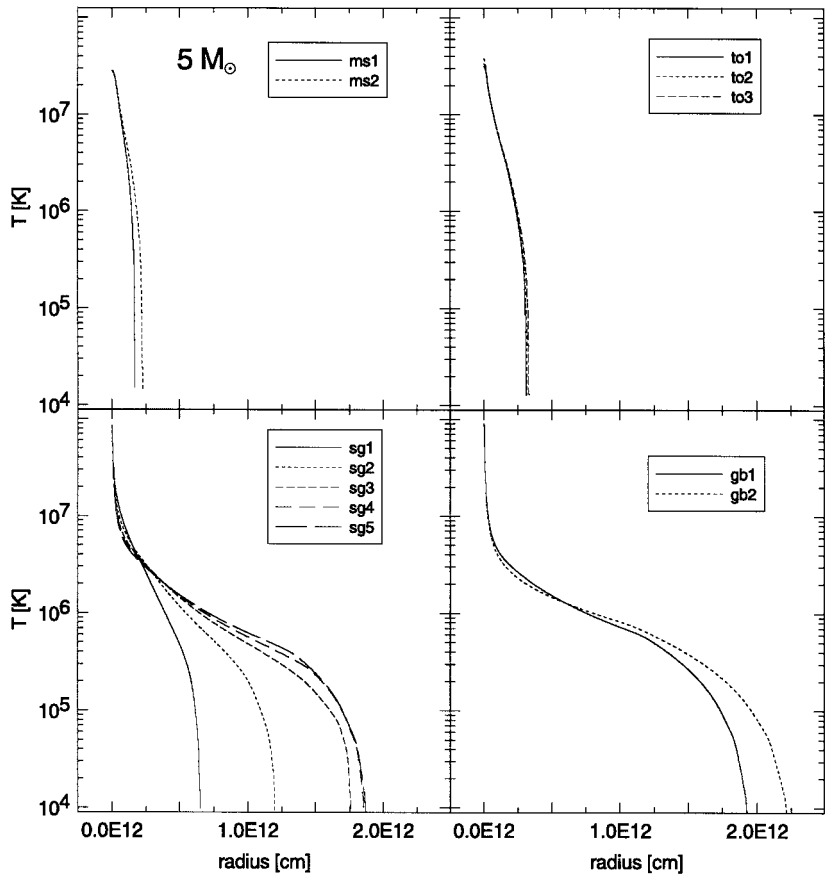

FIG. 7.—Temperature, T, vs. radius for the 5 $M_{\odot}$ models at 12 selected points along the evolutionary track of the star

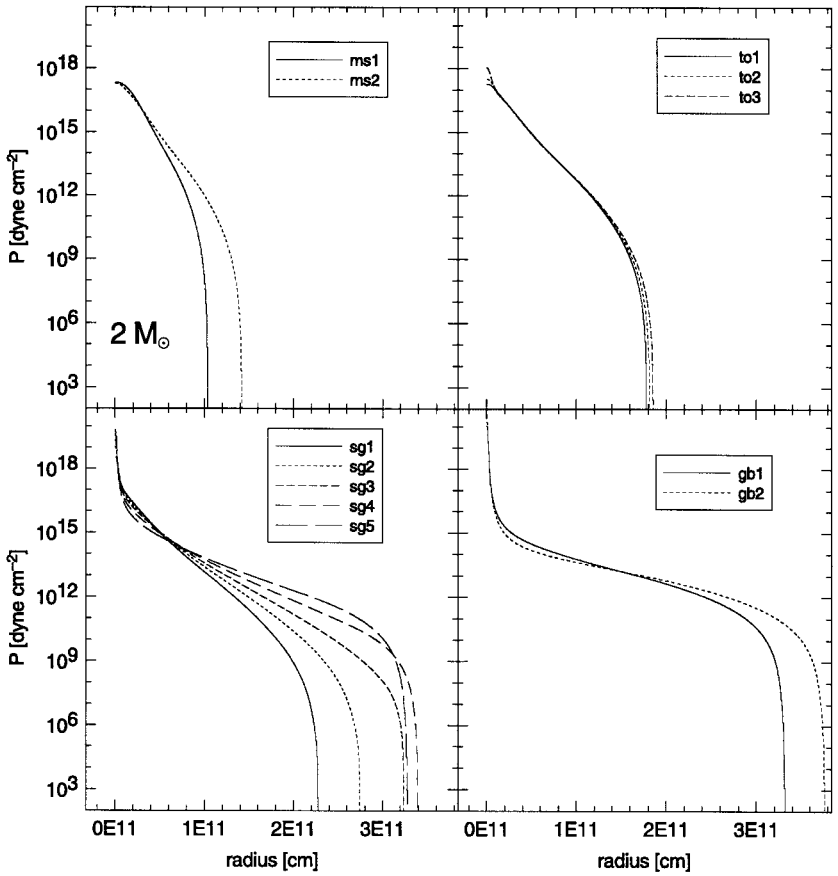

FIG. 8.—Pressure, P, vs. radius for the 2 $M_\odot$ models at 12 selected points along the evolutionary track of the star

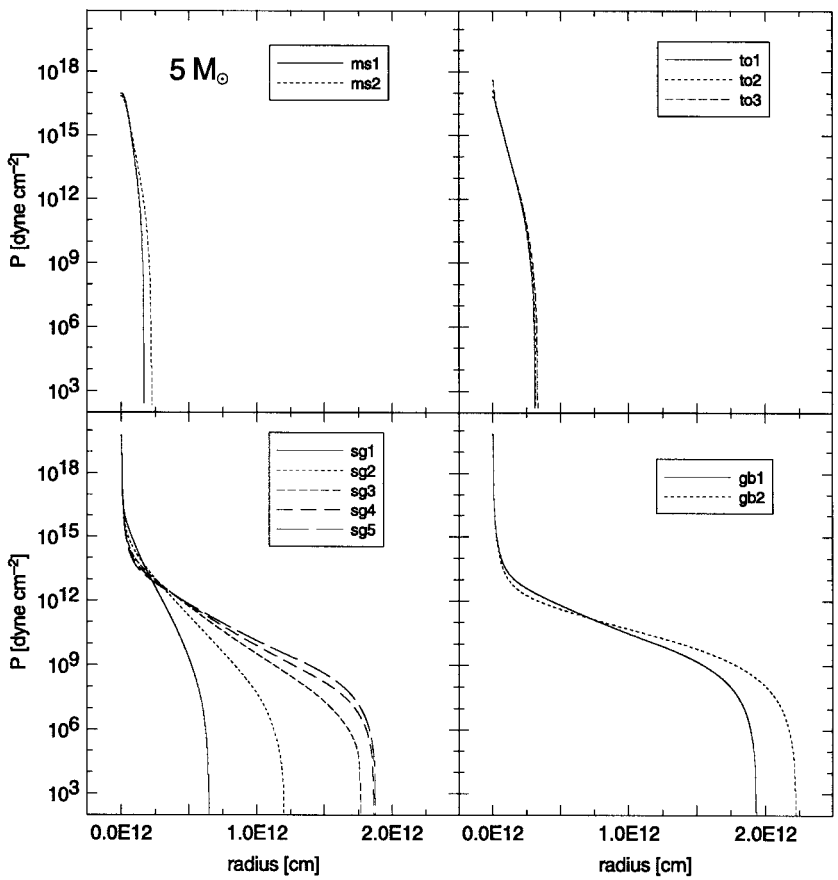

FIG. 9.—Pressure, P, vs. radius for the 5 $M_\odot$ models at 12 selected points along the evolutionary track of the star

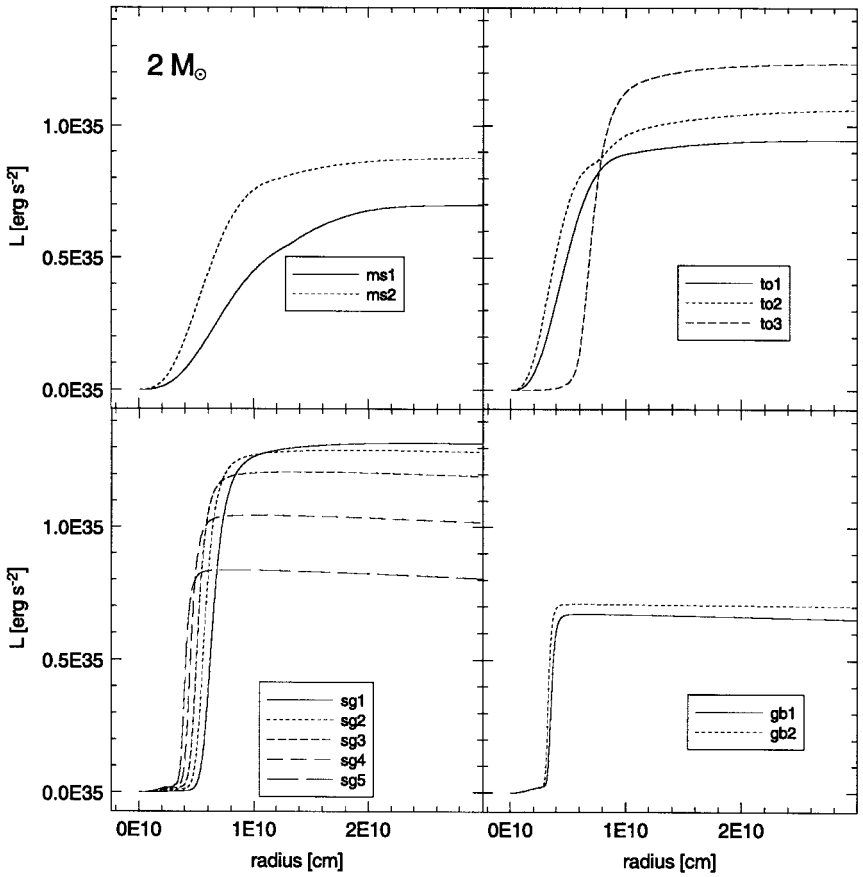

FIG. 10.—Luminosity, L, vs. radius for the 2 $M_{\odot}$ models at 12 selected points along the evolutionary track of the star

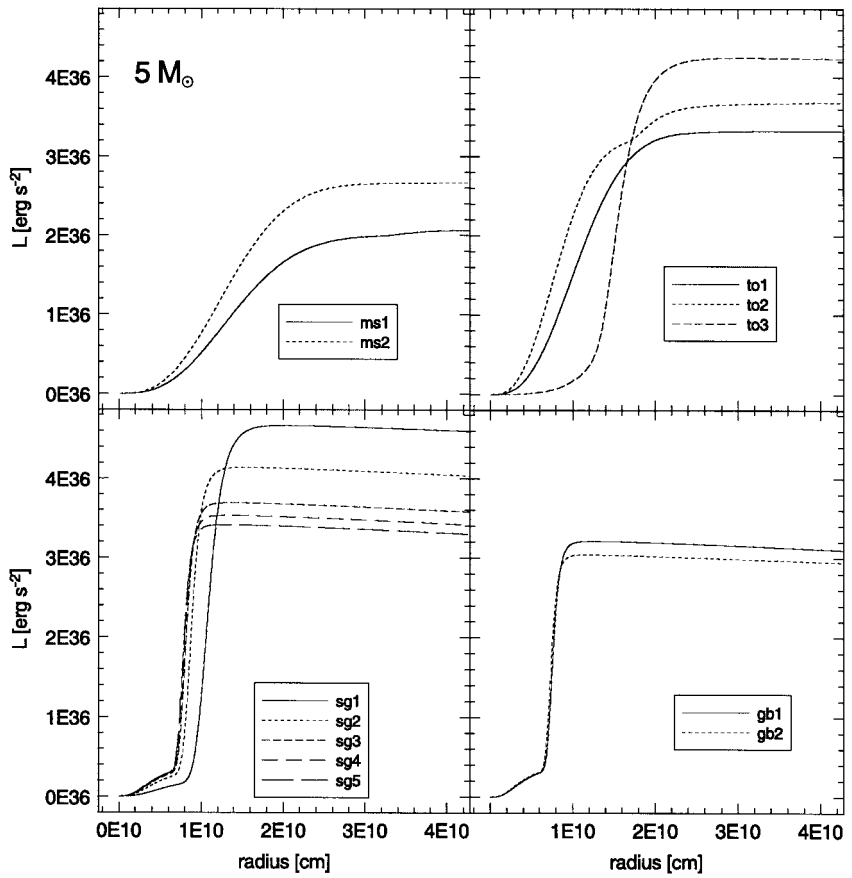

FIG. 11.—Luminosity, L, vs. radius for the 5 $M_{\odot}$ models at 12 selected points along the evolutionary track of the star

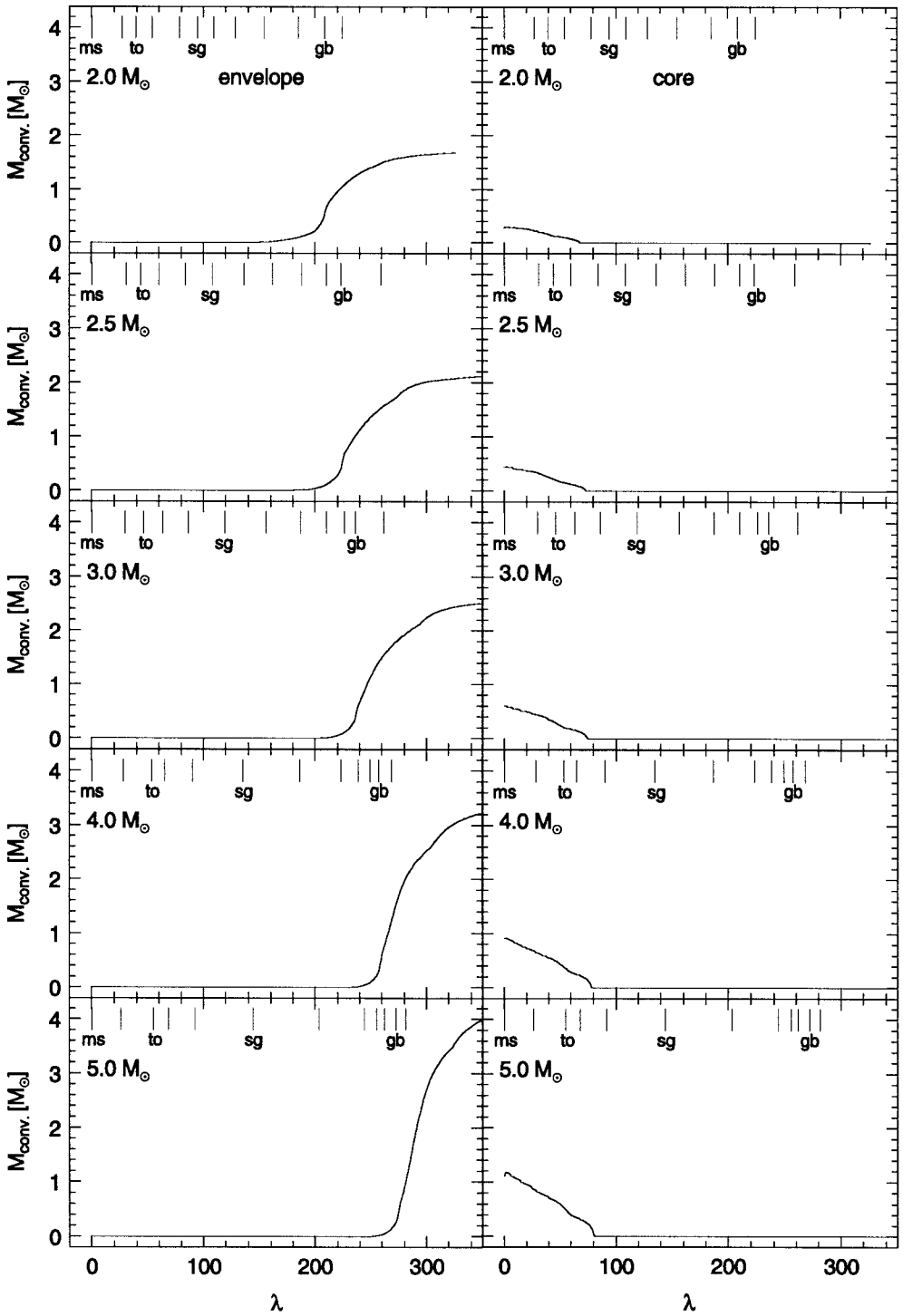

FIG. 12.—Convective envelope mass (*left-hand panels*) and convective core mass (*right-hand panels*) are plotted as functions of H-R diagram arc length, λ (see Fig. 3 for the relation between λ and age) for each of the intermediate-mass models. Hatch marks along the top of each panel identify the 12 selected points along each track.

4.4. *Convective Cores*

Stars in the mass range considered here are burning hydrogen primarily by the CNO cycle. The steep temperature dependence of the CNO nuclear luminosity concentrates most of the energy production in the centralmost regions. The energy from the core cannot escape by radiation alone, and the region becomes convective. The oscillation spectrum of a star is affected by the presence of a convective core since convection in the core alters the chemical composition of the core, when compared to a model without a convective core, by mixing in fresh hydrogen and by homogenizing the mixture of elements inside the mixed region. Since the chemical composition of the core out to the edge of the convective core is affected, the extent of the core can be probed by *p*-mode seismology. As the star evolves and the central regions become more concentrated, with the nuclear burning confined to an ever more centrally concentrated core, the convective core itself shrinks, leaving behind it a discontinuity in composition at its initial outer-

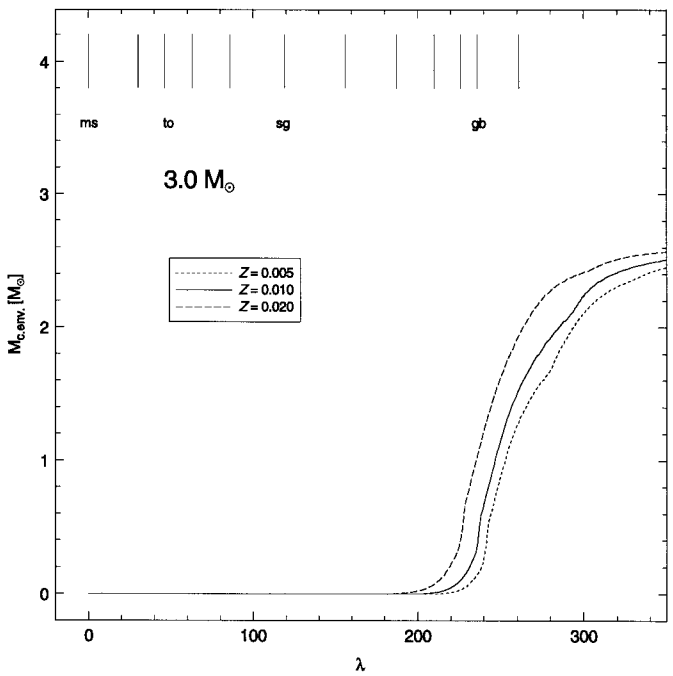

FIG. 13.—Convective envelope mass vs. λ for the 3 $M_\odot$ models with different metallicities, Z. Hatch marks along the top of each panel identify the 12 selected points along each track.

most extent. This has been noticed already in the interesting case of the binary star system α Cen AB (Guenther & Demarque 2000). The authors show that α Cen A is at a critical phase of evolution where models with very slight differences can have or not have convective cores. Whether α Cen A does have a convective core will be revealed when its oscillation spectrum is observed. Of specific interest would be whether or not the extent of the convective core matches theoretical predictions or, more specifically, whether or not convective overshoot is required in the model. Convective core overshoot extends the main-sequence lifetime of a star. For stars in the mass range considered here, the convective core disappears before the convective envelope appears; hence, the stars in this mass range are unlikely to have observable p-modes at the same time that the stars are predicted to have convective cores.

4.5. *Mean Molecular Weight, Adiabatic Exponent, and Sound Speed*

Although the variables ρ, P, T, and L describe the overall structure and evolution of a star, other derived quantities have a more direct connection to stellar pulsation, specifically, the mean molecular weight, μ, the adiabatic exponent, Γ_1, the sound speed, c, the Brunt-Väisälä frequency, and the Lamb frequency.

The mean molecular weight and the adiabatic exponent undergo significant changes in the outer regions of the star where p-mode oscillation modes are most sensitive. The mean molecular weight is defined as the average mass of all the atomic particles, including electrons, in units of the mass of a hydrogen ion. Throughout most of the interior of a star, where hydrogen and helium are complete ionized, $\mu \cong (2X + 0.75Y)^{-1} \cong 0.6$. Variations in the mean molecular weight in the envelope of a star can be traced to variations in the number fraction of electrons, especially near the H and He ionization regions. The adiabatic exponent is defined by $\Gamma_1 = (\partial \ln p/\partial \ln \rho)|_S$, that is, the logarithmic derivative of log pressure with respect to density at constant entropy, S. The term Γ_1 remains relatively constant in the interior, at approximately 5/3, undergoing changes near the surface, where it follows the changes in mean molecular weight. The adiabatic sound speed depends on both the mean molecular weight and the adiabatic constant ($c^2 = \Gamma_1 P/\rho$). The sound speed decreases with increasing radius in a star. The p-mode frequencies are inversely proportional (to leading order; see § 5.1) to the inverse sound speed integrated over the radius of the star. As the sound speed decreases, its contribution to the integral increases; hence, the greatest sensitivity of the p-mode frequencies occurs in the outer layers where small perturbations to the sound speed are most strongly felt.

In Figures 14, 15, and 16 we plot the mean molecular weight versus radius fraction near the surface for the 2, 3, and 5.0 $M_\odot$ models at the 12 selected phases of evolution. As μ runs outward through the H and He ionization zones, it undergoes step increases as the number of electrons decreases first through the helium ionization zones, then through the hydrogen ionization zone. The surface temperature of the 3 and 5 $M_\odot$ models does not drop below 10,000 K (see Fig. 1), the ionization temperature of H, until after turnoff; hence, μ does not show the last step increase (corresponding to the H ionization region) for these models. Note that convection does not smooth out the steps since ionization occurs on a much shorter timescale than convection.

In Figures 17, 18, and 19 we show the adiabatic exponent versus radius fraction for the 2, 3, and 5.0 $M_\odot$ models at the 12 selected phases of evolution. And in Figures 20, 21, and 22 we show the same quantities but on an expanded scale near the surface. The structure of Γ_1 is quite complicated. Without modern computations of the atomic physics in the form of opacity tables and equation-of-state tables (especially from Lawrence Livermore), from which we obtain μ and Γ_1, it would not be possible to carry out the structural inversions of p-mode data to any useful degree of accuracy.

The sound speed decreases from the center of a star outward (see Figs. 23, 24, and 25). There is a sharp bump in the sound speed near the inner boundary of the hydrogen-burning shell, noticeable in the post–main-sequence models (e.g., ms2). This is where there is an abrupt drop in mean molecular weight, as one moves outward from the isothermal helium core to the surrounding regions. Because the convective core edge moves inward as the star evolves, it leaves behind a discontinuity in composition where the convective core reached its maximum extent. The location and size of the bump depend on the rate of nuclear burning in the core and the evolution of the convective core edge. Its effect on the p-modes can be seen in the p-mode oscillation spectra (especially through the small spacing discussed in § 5).

4.6. *Brunt-Väisälä and Lamb Frequencies*

Many basic characteristics of the oscillation properties of a star can be understood through plots of the Brunt-Väisälä, N, and Lamb, L_l, frequencies (see Unno et al. 1979). The Brunt-Väisälä frequency corresponds to the fundamental buoyancy frequency at a given shell in the model; that is, it is the frequency at which a displaced fluid element will oscillate adiabatically about its equilibrium position. In convective regions a displaced fluid element, by definition, does not

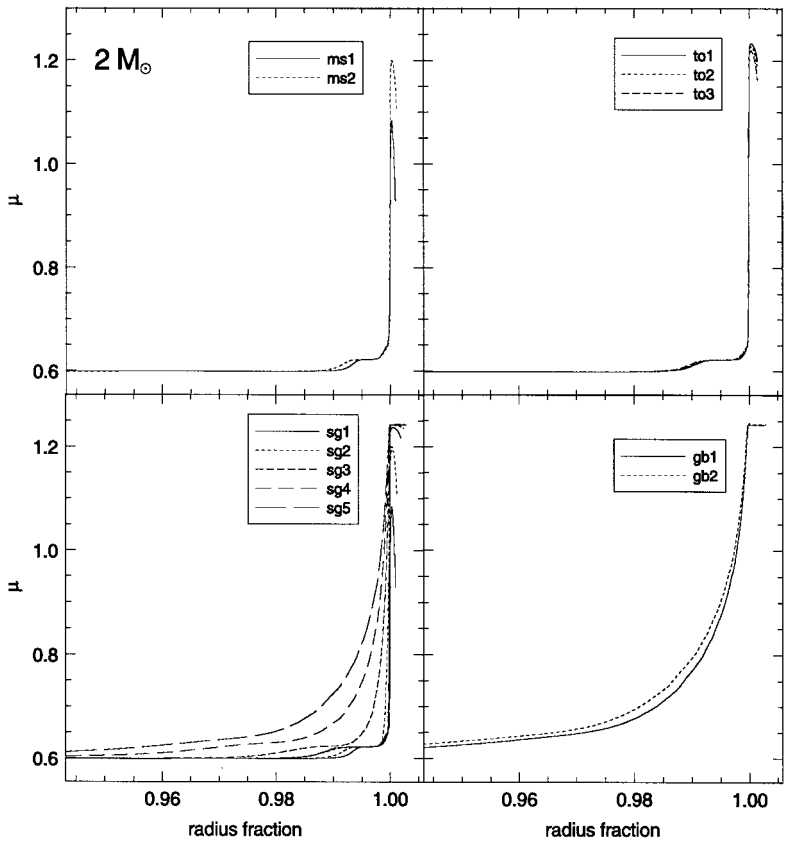

FIG. 14.—Mean molecular weight, μ, vs. radius for the 2 $M_\odot$ models at 12 selected points along the evolutionary track of the star

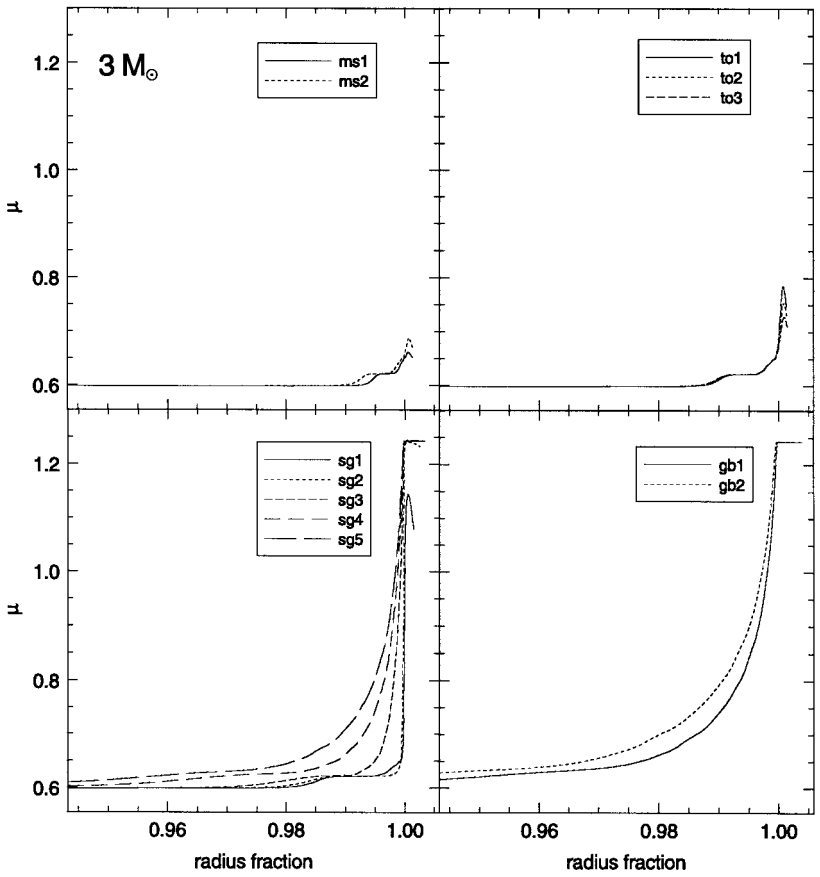

FIG. 15.—Mean molecular weight, μ, vs. radius for the 3 $M_\odot$ models at 12 selected points along the evolutionary track of the star

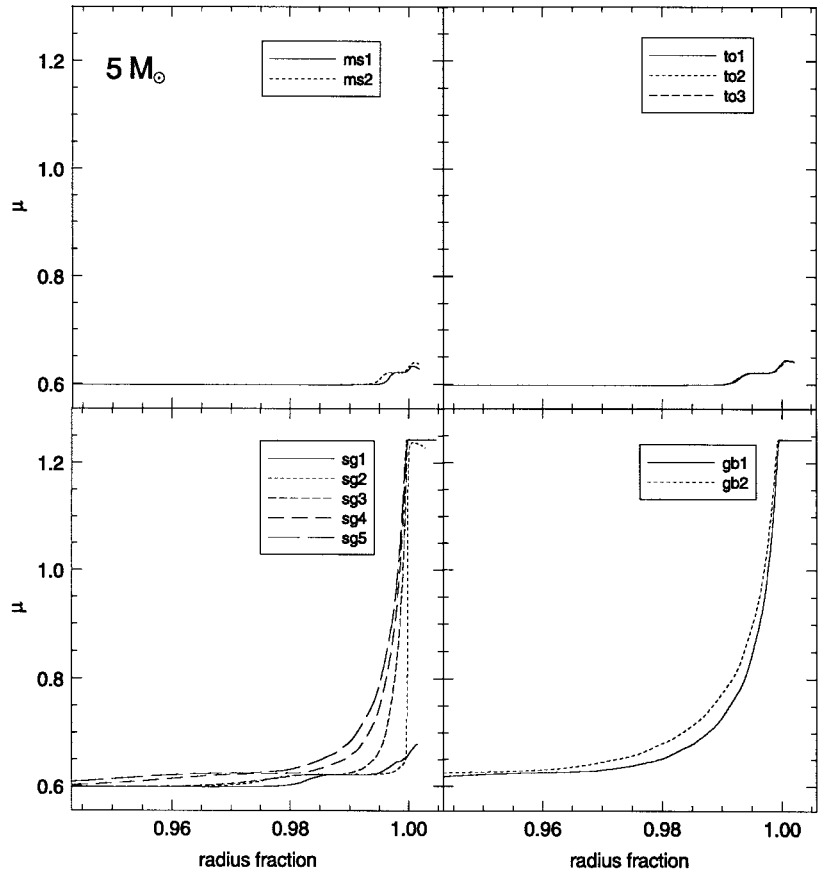

FIG. 16.—Mean molecular weight, μ, vs. radius for the 5 $M_\odot$ models at 12 selected points along the evolutionary track of the star

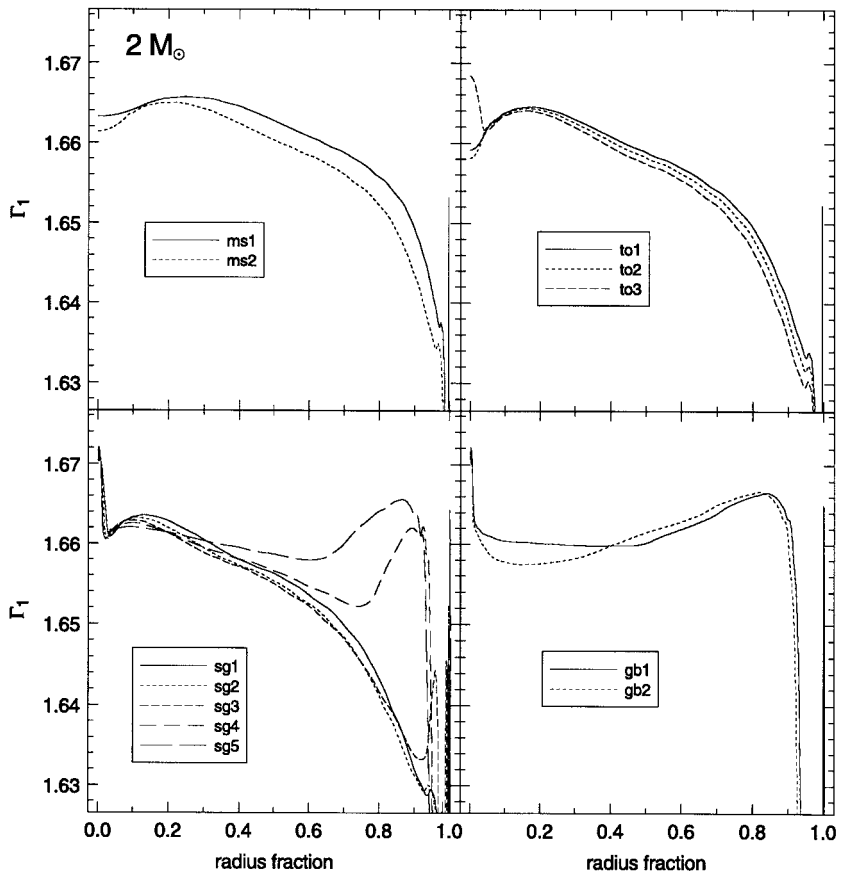

FIG. 17.—Adiabatic exponent, Γ_1, vs. radius for the 2 $M_\odot$ models at 12 selected points along the evolutionary track of the star

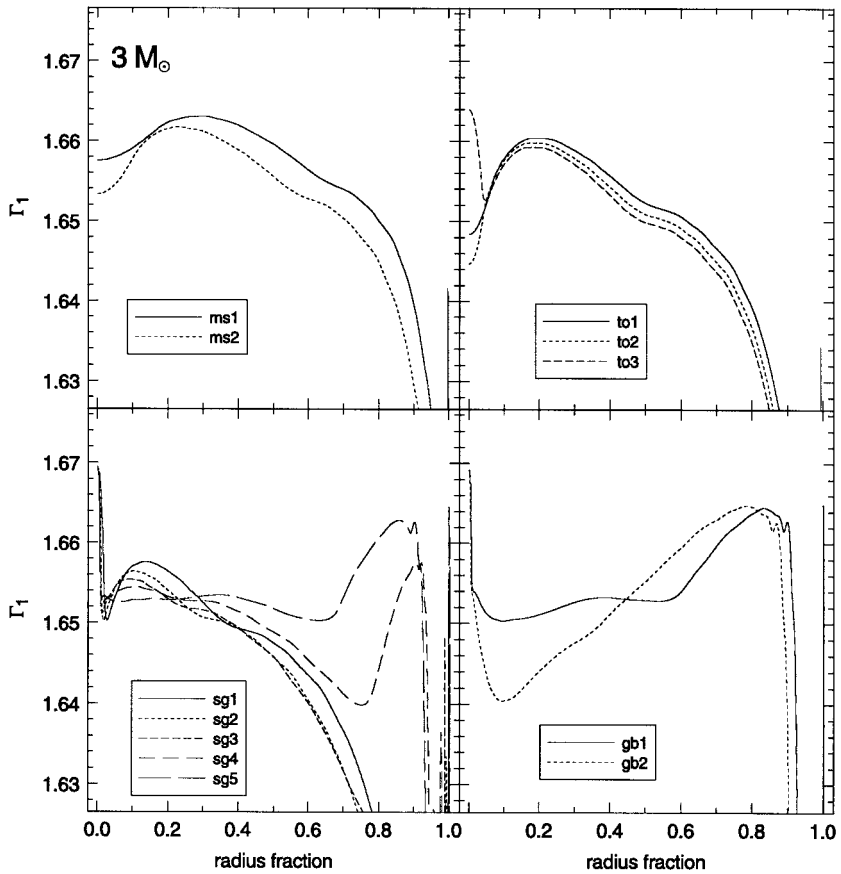

FIG. 18.—Adiabatic exponent, Γ_1, vs. radius for the 3 $M_\odot$ models at 12 selected points along the evolutionary track of the star

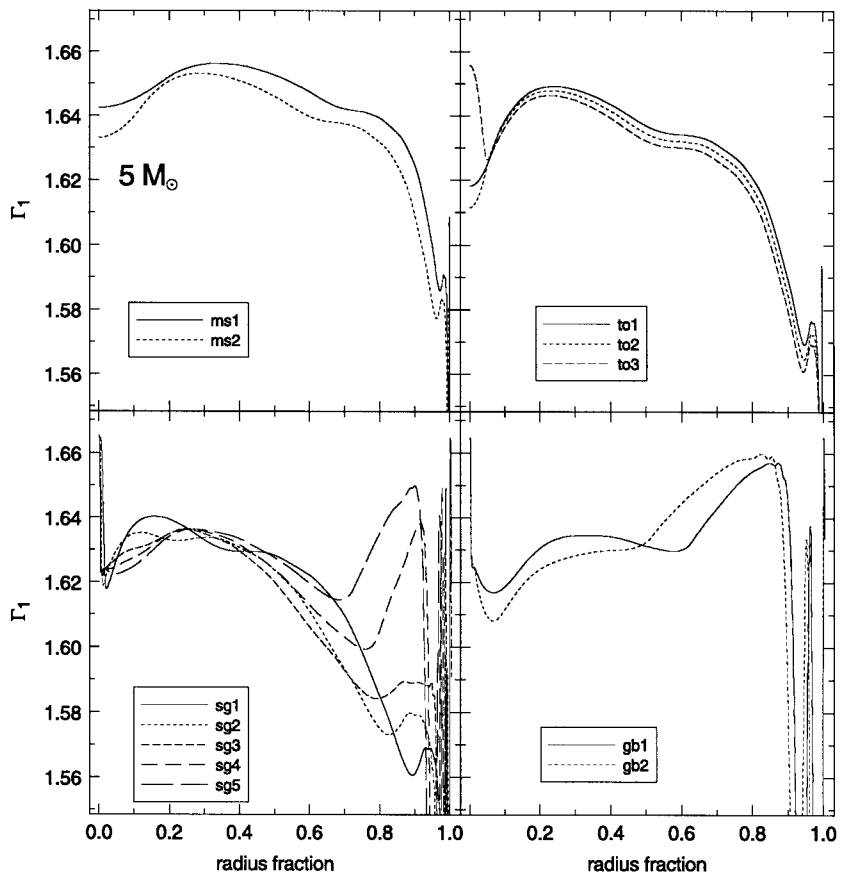

FIG. 19.—Adiabatic exponent, Γ_1, vs. radius for the 5 $M_\odot$ models at 12 selected points along the evolutionary track of the star

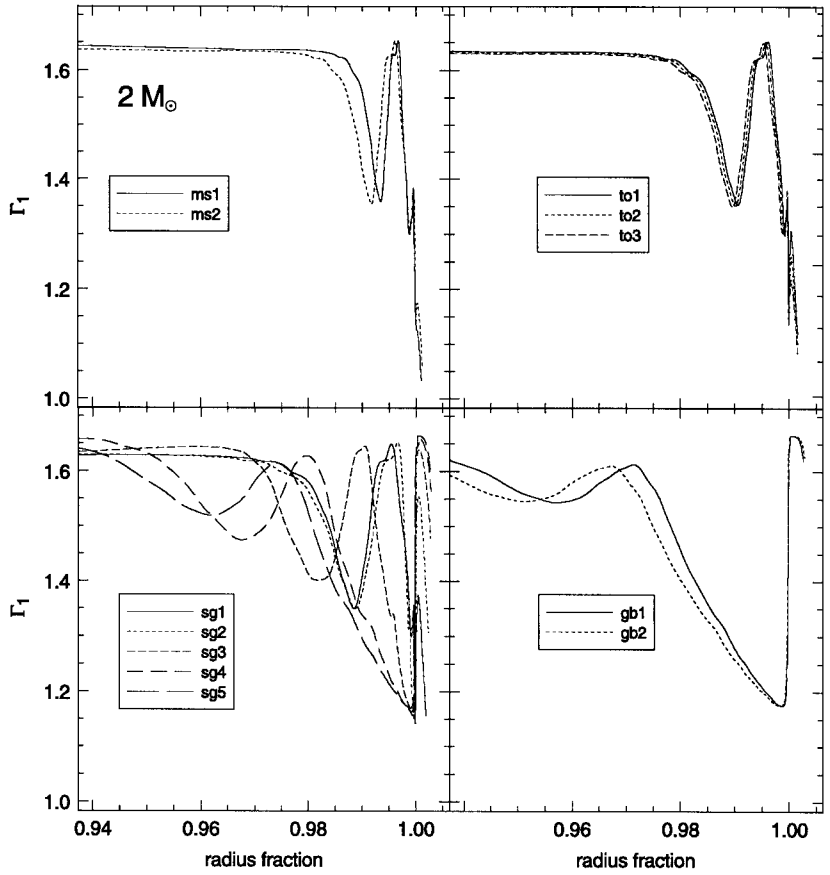

FIG. 20.—Adiabatic exponent, Γ_1, vs. radius near the surface for the 2 $M_\odot$ models at 12 selected points along the evolutionary track of the star

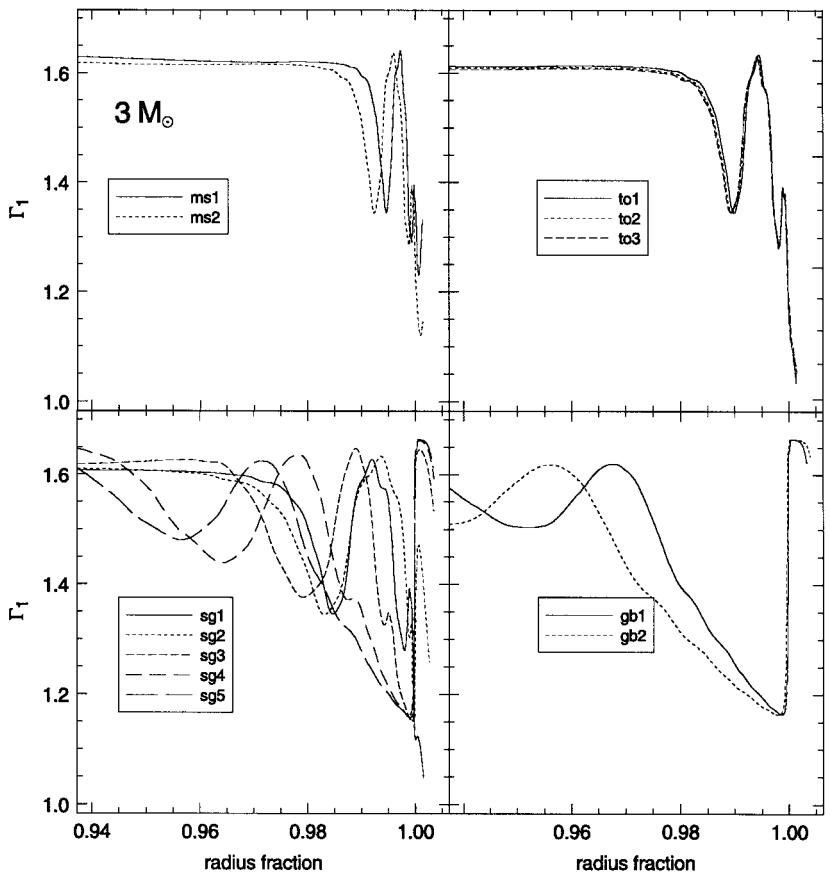

FIG. 21.—Adiabatic exponent, Γ_1, vs. radius near the surface for the 3 $M_\odot$ models at 12 selected points along the evolutionary track of the star

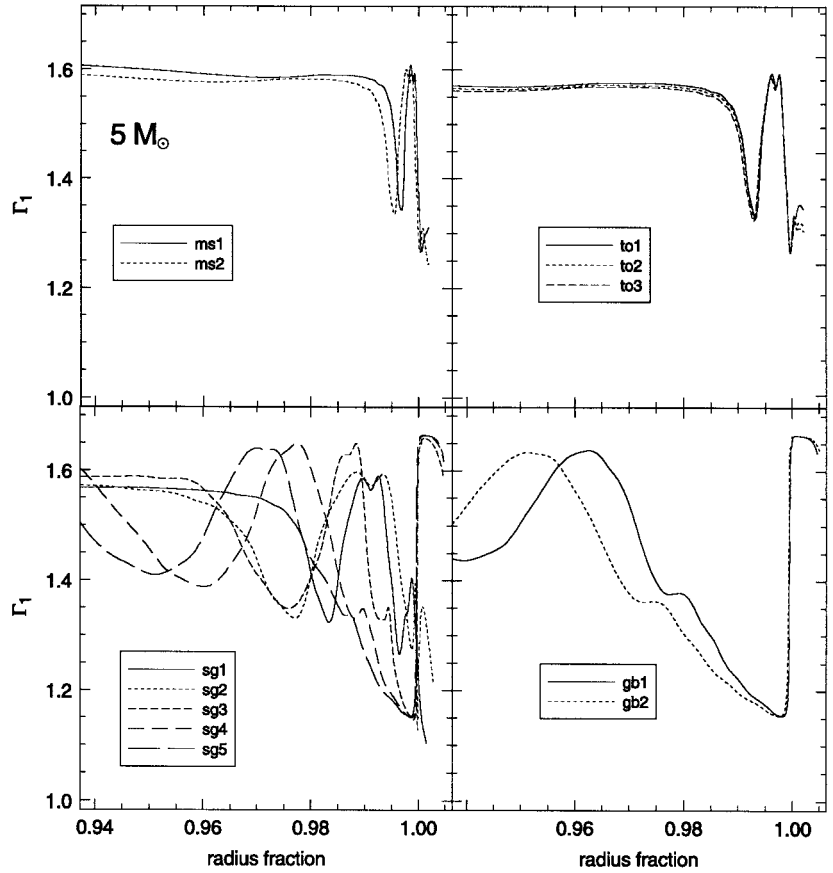

FIG. 22.—Adiabatic exponent, Γ_1, vs. radius near the surface for the 5 $M_\odot$ models at 12 selected points along the evolutionary track of the star

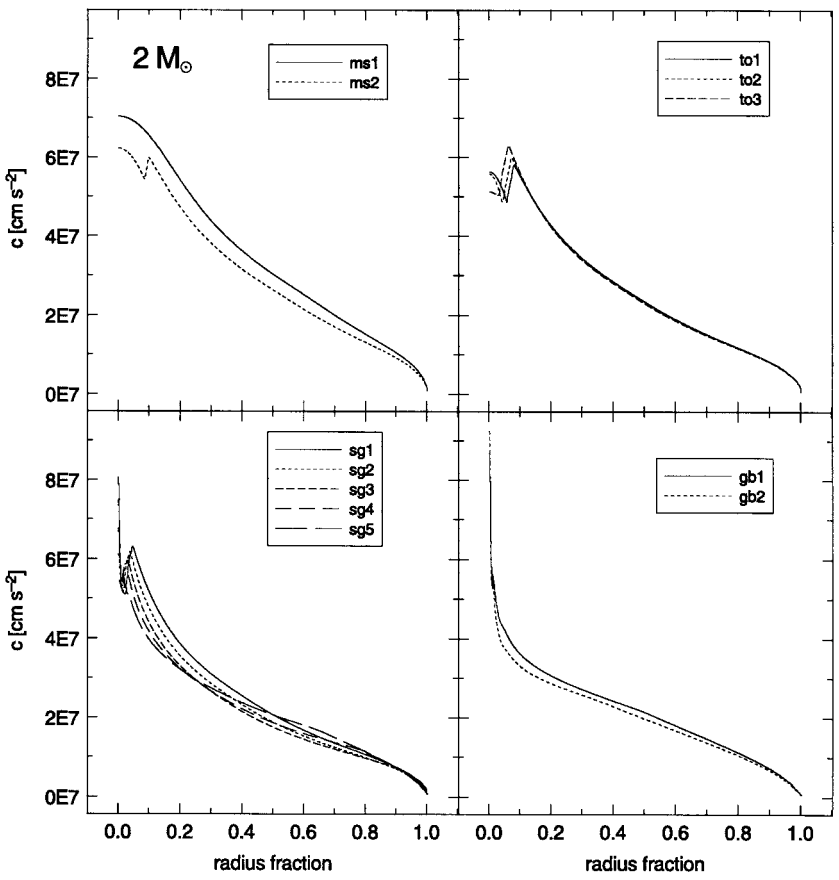

FIG. 23.—Sound speed, c, vs. radius for the 2 $M_\odot$ models at 12 selected points along the evolutionary track of the star

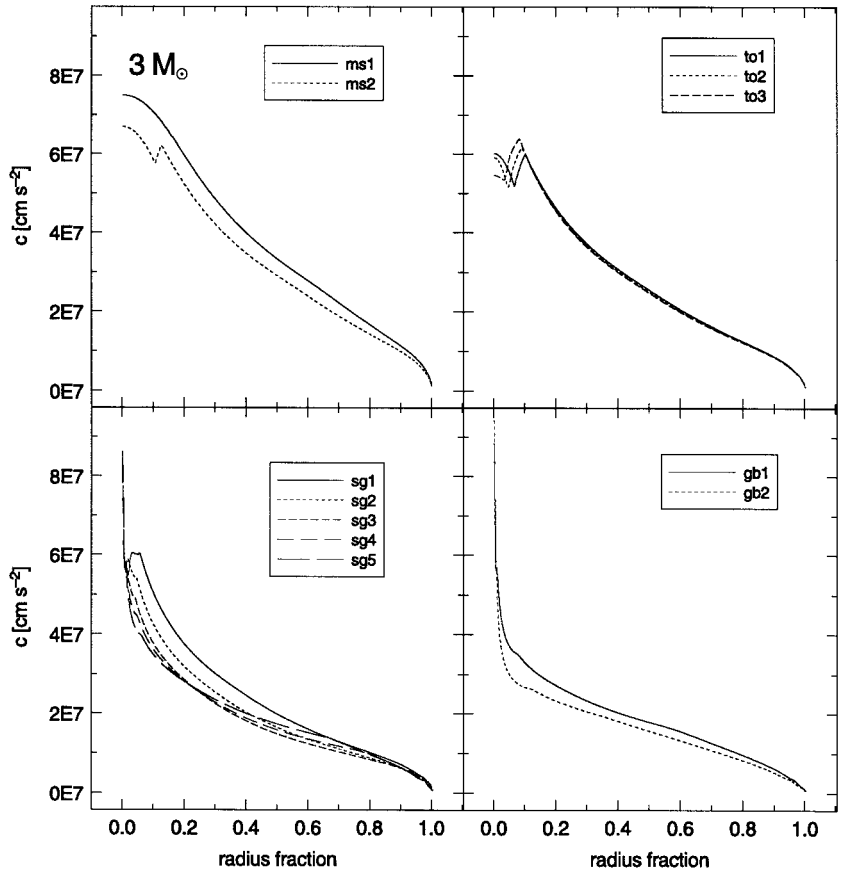

FIG. 24.—Sound speed, c, vs. radius for the 3 $M_\odot$ models at 12 selected points (see Fig. 1) along the evolutionary track of the star

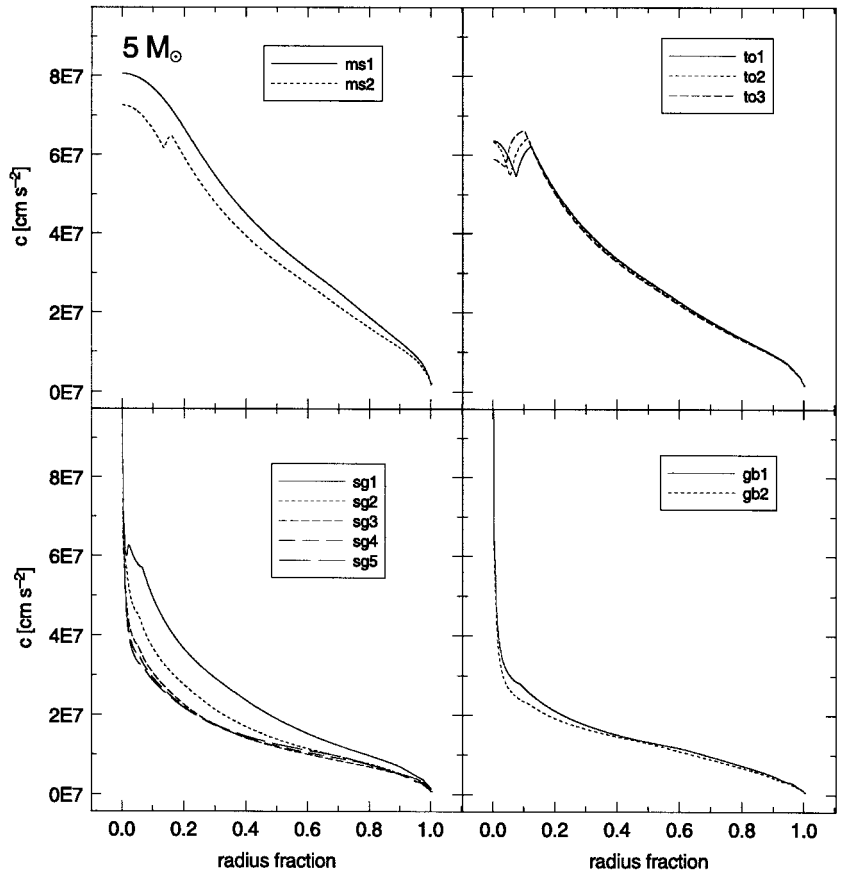

FIG. 25.—Sound speed, c, vs. radius for the 5 $M_\odot$ models at 12 selected points (see Fig. 1) along the evolutionary track of the star

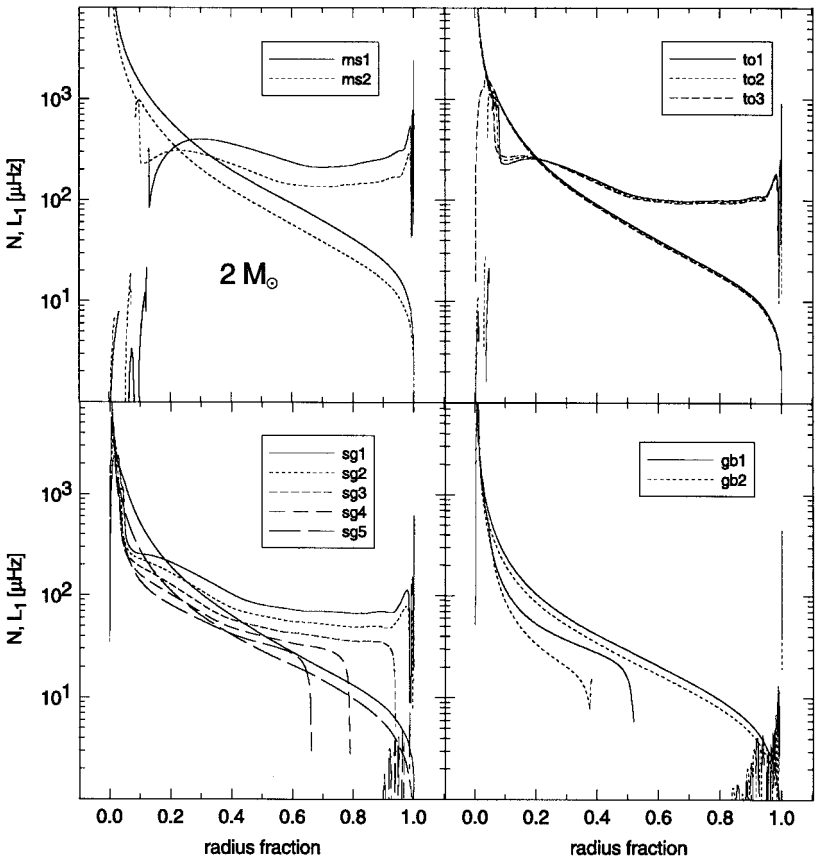

FIG. 26.—Brunt-Väisälä frequency, N, and the Lamb frequency, L_1, vs. radius for the 2 $M_\odot$ models at 12 selected points along the evolutionary track of the star. The curves corresponding to the Lamb frequency sweep smoothly from the upper left corner to the lower right corner of each plot.

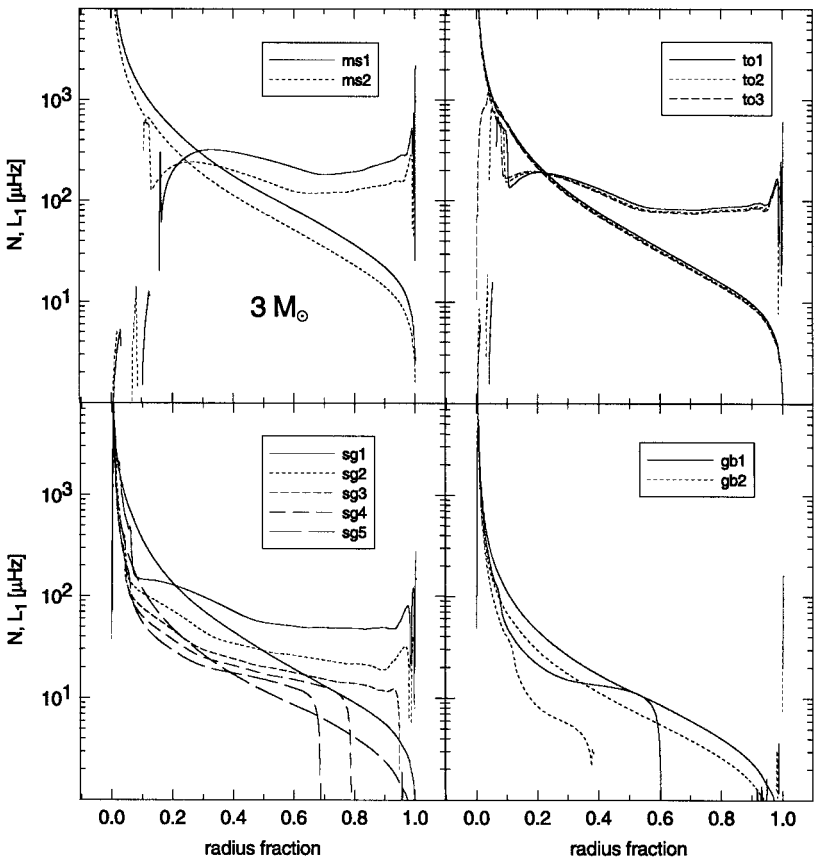

FIG. 27.—Brunt-Väisälä frequency, N, and the Lamb frequency, L_1, vs. radius for the 3 $M_\odot$ models at 12 selected points along the evolutionary track of the star.

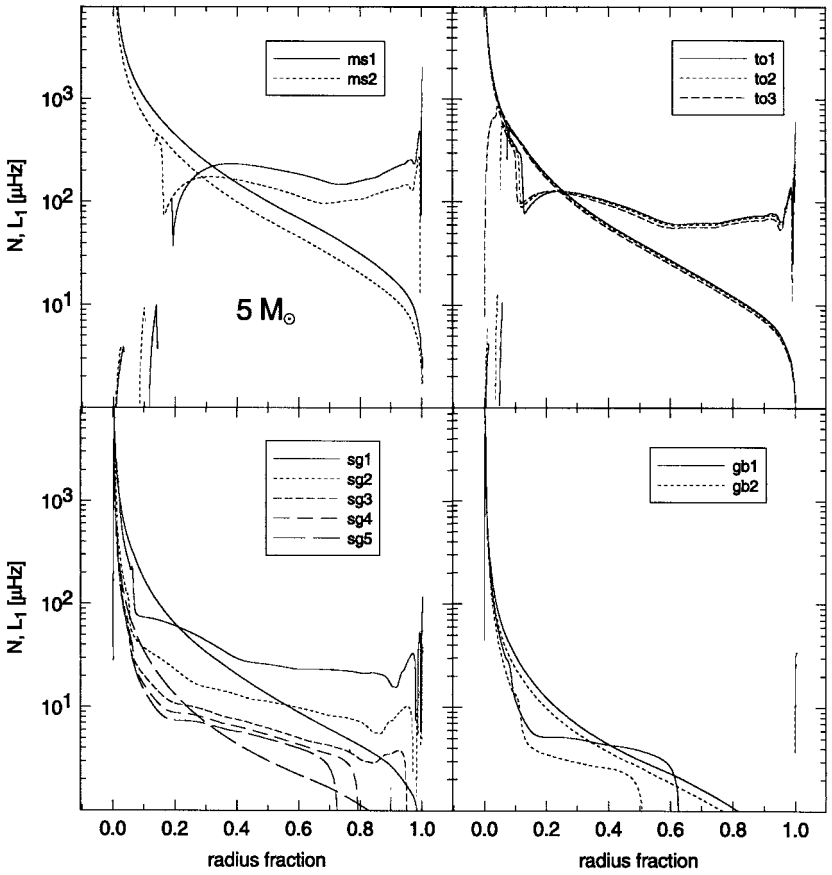

FIG. 28.—Brunt-Väisälä frequency, N, and the Lamb frequency, L_1, vs. radius for the 5 $M_\odot$ models at 12 selected points along the evolutionary track of the star.

return to its equilibrium position but continues to rise or fall from its displaced position; that is, the perturbed displacement grows exponentially. In convective regions the square of the Brunt-Väisälä frequency is negative; hence, the frequency itself is imaginary. For plotting purposes we set the Brunt-Väisälä frequency to zero in these regions. The Lamb frequency corresponds to the frequency of a horizontal acoustic wave of wavelength $2\pi r/l$. Acoustic modes (p-modes) propagate in regions where the oscillation frequency is greater than both the Brunt-Väisälä and Lamb frequencies. The p-modes are evanescent in other regions. Gravity modes (g-modes) propagate in regions where the oscillation frequency is less than both the Brunt-Väisälä and Lamb frequencies.

Figures 26, 27, and 28 show N and $L_{l=1}$, in units of microhertz, versus radius fraction at the 12 selected phases of evolution for the 2, 3, and 5 $M_\odot$ models, respectively. As the star evolves off of the main-sequence, helium is built up in the core. This produces a bump in the Brunt-Väisälä frequency in the core. Since the bump lies below the Lamb frequency in this region, g-modes can exist in this region. Indeed, the frequencies of the g-modes in this region overlap the frequencies of the p-modes outside this region. The presence of g-modes at frequencies near the p-modes perturbs the p-mode frequencies. The effect is visible in the oscillation spectrum of a star as unequal large spacings for the low–n-value p-modes. The surface convection zone is also revealed in the propagation diagrams. The Brunt-Väisälä frequency drops quickly to zero (becomes imaginary) in the convective regions. As the star evolves to the right in the H-R diagram toward cooler surface temperatures, models sg1–sg5, a convective envelope develops and deepens. In these models, the Brunt-Väisälä frequency is seen to abruptly drop to zero at the base of the convective envelope.

5. OSCILLATION PROPERTIES

5.1. *Introduction*

Tassoul (1980) has derived a useful asymptotic formula for the p-mode frequencies, commonly written as

$$\nu_{nl} \cong \left(n + \frac{l}{2} + \frac{1}{4} + \beta\right)\Delta\nu - (AL^2 - \varepsilon)\frac{\Delta\nu^2}{\nu_{nl}} ,$$

where

$$\Delta\nu = \left(2\int_0^R \frac{dr}{c}\right)^{-1} ,$$

$$A = \frac{1}{4\pi^2\Delta\nu}\left(\kappa - \int_0^R \frac{dc}{dr}\frac{dr}{r}\right) .$$

The constants β, ε, and κ depend on the structure of the surface layers. The variable n is the radial order of the mode, l is the azimuthal order of the mode, c is the speed of sound, R is the radius of the star, and $L = l + 1/2$. The asymptotic formula clearly shows that the oscillation frequencies depend on the run of sound speed.

It is easy to isolate the first- and second-order terms in the asymptotic expression by forming specific differences of the frequencies. The large frequency spacing, defined as

$$\Delta_n \equiv \nu_{nl} - \nu_{n-1,l} \propto \Delta\nu \ ,$$

is to leading order (assuming $n \gg l$) proportional to $\Delta\nu$, which depends on the sound speed predominately in the surface layers. The small frequency spacing, defined as

$$\delta_n \equiv \nu_{nl} - \nu_{n-1,l+2} \propto \Delta\nu \int_0^R \frac{dc}{dr}\frac{dr}{r} \ ,$$

isolates the second-order term, which depends predominately on the sound speed (its derivative) in the interior.

When oscillation spectra of stars are observed, it is expected that the spectra will initially reveal the large and small spacings, from a Fourier transform of the power spectrum. The large and small spacings characterize the regular spacing of the p-modes. The utility of the large and small spacings decreases for stars that have evolved beyond the main sequence. Here, mode bumping of p-modes by g-modes perturbs the frequencies to such an extent that the regular spacing of the modes disappears. Indeed, by the time the star arrives at the base of the giant branch, only radial ($l = 0$) p-modes hold any semblance of regular spacings (Guenther & Demarque 2000).

Even though we do not expect that stars with masses between 2 and 5 $M_\odot$ to have visible p-mode spectra until they develop convective envelopes during their approach to the giant branch, it is instructive to study the theoretical p-mode oscillation spectra of these stars during all phases of their evolution. Furthermore, because the internal dynamical properties of intermediate and massive stars are still not fully understood, it is possible that mechanisms, other than turbulent convection at the surface, exist to drive the acoustic oscillations in these stars.

Along each stellar evolutionary track, consisting of a sequence of ~2500 models, several hundred equally spaced (in the H-R diagram) models were selected for pulsation analysis. The models were input into Guenther's nonadiabatic, nonradial stellar pulsation code (Guenther 1994). The code solves the linearized pulsation equations by relaxation. The nonadiabatic terms describe radiative gains and losses in the Eddington approximation and hence are valid in regions of low optical depth. Perturbations to the convective flux are neglected. All $l = 0$, 1, and 2 p-modes with n ranging from 0 to 35 were calculated.

Table 2 lists some of the pulsation properties of the 12 selected models along each track.

5.2. *Large Spacing*

The large spacing $\Delta_{n,l}$ is primarily an indicator of stellar radius. What is remarkable is how insensitive it is to other parameters of the stellar model, including mass. In Figure 29 we plot $\langle\Delta_{n,l}\rangle_{l=0}$ versus stellar radius R for all the models that have been pulsed. Here $\langle\Delta_{n,l}\rangle_{l=0}$ is the average large spacing for $n = 10$–20 and $l = 0$. With an observed $\Delta_{n,l}$, suitably averaged, one can read off an approximate measure of the radius of the star from Figure 29. The term $\langle\Delta_{n,l}\rangle$ does depend slightly on mass, increasing for increasing mass at a given radius. In Figure 30 we plot $\langle\Delta_{n,l}\rangle_{l=0}$ versus stellar radius for 3 $M_\odot$ stars of varying metallicity to show that $\langle\Delta_{n,l}\rangle_{l=0}$ is insensitive to Z. Similar plots (not shown) for varying Y and α reveal even less sensitivity to these parameters for stars between 2 and 5 $M_\odot$. In other words, $\langle\Delta_{n,l}\rangle$ makes an excellent measure of stellar radius regardless of stellar evolutionary phase, mass, or composition.

The term $\langle\Delta_{n,l}\rangle$ is approximately inversely proportional to radius, and this relationship is maintained without much variation for all the models considered here. The proportionality constant, though, does vary through different phases of evolution as shown in Figure 31, which plots $R\langle\Delta_{n,l}\rangle_{l=0}$ versus age.

The large spacing can be obtained from a Fourier transform of the power oscillation spectrum of a star. The dominant peak in the transform corresponds to one-half the large spacing for stars near the main sequence (the odd and even l p-mode frequencies are displaced by one-half the large spacing) and corresponds to the large spacing itself for stars in more advanced phases of evolution, where only the radial modes remain regularly spaced. Of course, when high-quality oscillation spectra are obtained from stars that permit individual modes to be identified, $\langle\Delta_{n,l}\rangle$ can be calculated directly.

We have calculated the large spacing by averaging the large spacings over a range in n. The average value of $\langle\Delta_{n,l}\rangle$ does depend on the range of n chosen. Interestingly, this dependence on n itself depends on mass. We define $\Delta\langle\Delta_{n,l}\rangle$ as the difference between $\langle\Delta_{n,l}\rangle$ averaged over $n = 10$–20 and $\langle\Delta_{n,l}\rangle$ averaged over $n = 5$–10. Figure 32 shows a plot of $\Delta\langle\Delta_{n,l}\rangle$ versus H-R diagram arc length, λ, for all of the pulsed models. The large dots along each curve identify the 12 selected phases of evolution. The plot shows that $\Delta\langle\Delta_{n,l}\rangle$ depends on the mass of the star and that it is especially sensitive, at the 2% level, for masses between 2 and 3 $M_\odot$. Not shown here, models of stars with lower mass, which we have calculated, also show a dependence of $\Delta\langle\Delta_{n,l}\rangle_n$ on mass. We suggest that $\Delta\langle\Delta_{n,l}\rangle_n$ may be useful as a mass indicator for stars with masses less than 3 $M_\odot$. Note, though, as we show in Figure 33, that for a 3 $M_\odot$ model, $\Delta\langle\Delta_{n,l}\rangle$ is also sensitive to Z. Further analysis is required to establish the true utility of this parameter.

5.3. *Small Spacing*

The small spacing is sensitive to the structure of the core, and, for this reason, it is sensitive to the state of evolution of the star. In Figure 34*a* we plot the small spacing $\langle\delta_{n,l}\rangle_{l=0}$ averaged over $n = 10$–20, $l = 0$, for all of the pulsed models. Dots along the curves correspond to the 12 selected phases of evolution beginning with ms1 at the top left and continuing in sequence along each curve. The small spacing decreases as the model evolves and the core density increases. Because mode bumping destroys the regular spacing between nonradial modes, the small spacing is not well defined beyond turnoff. In order to use the small spacing as an age indicator, one must know the composition of the star because the small spacing is also sensitive to Y and Z. In Figures 34*b* and 34*c*, we plot the small spacing for the 3 $M_\odot$ models at different metallicities and helium abundances, respectively. Figures 34*b* and 34*c* show that at a given age, the small spacing depends on composition. We note again that because stars in the mass range 2–5 $M_\odot$ do not have convective envelopes prior to turnoff, they are not predicted to have observable p-mode oscillation spectra; hence, the

TABLE 2

SELECTED MODEL PULSATION PROPERTIES

Mass $M_\odot$ (1)	Label (2)	$\Delta_0(5–10)$ (3)	$\Delta_0(10–20)$ (4)	$\Delta_1(5–10)$ (5)	$\Delta_1(10–20)$ (6)	$\delta_0(5–10)$ (7)	$\delta_0(10–20)$ (8)
2.0.....	ms1	91.76	93.56	91.54	93.36	8.83	11.19
2.0.....	ms2	56.55	59.23	57.28	59.33	4.94	5.26
2.0.....	to1	40.29	43.05	40.27	42.97	5.19	3.62
2.0.....	to2	39.13	41.73	47.24	41.74	4.54	4.75
2.0.....	to3	37.90	40.48	38.62	36.73		3.79
2.0.....	sg1	28.44	30.58	44.47	30.15		
2.0.....	sg2	22.28	23.94		19.34		
2.0.....	sg3	18.59	19.30	34.86	36.83		
2.0.....	sg4	17.81	18.54	34.50	36.67		
2.0.....	sg5	18.98	19.45	38.90			
2.0.....	gb1	18.54	18.80	8.46			
2.0.....	gb2	15.11	15.47				
2.5.....	ms1	87.32	87.94	86.83	87.67	8.73	10.92
2.5.....	ms2	54.05	54.86	54.24	54.97	4.69	4.96
2.5.....	to1	36.34	37.76	36.36	37.75	4.76	3.31
2.5.....	to2	34.89	36.27	35.05	36.20	3.91	3.82
2.5.....	to3	33.61	35.04	27.38	31.82		3.38
2.5.....	sg1	21.42	22.70	17.80	18.59		
2.5.....	sg2	14.46	15.41	18.94	9.40		
2.5.....	sg3	11.44	11.87	10.61			
2.5.....	sg4	11.34	11.80	12.72			
2.5.....	sg5	12.08	12.51				
2.5.....	gb1	11.85	12.21				
2.5.....	gb2	7.68	8.02				
3.0.....	ms1	82.55	83.03	81.98	82.84	8.57	10.57
3.0.....	ms2	51.42	51.76	51.53	51.87	4.68	4.84
3.0.....	to1	34.32	34.83	34.56	34.98	4.44	2.89
3.0.....	to2	32.25	32.82	32.38	32.77	3.28	7.21
3.0.....	to3	31.29	32.10	22.67	30.21		5.03
3.0.....	sg1	16.87	17.64	13.22	25.33		
3.0.....	sg2	10.35	10.99		6.56		
3.0.....	sg3	7.79	8.05	6.53			
3.0.....	sg4	7.68	7.97	11.89			
3.0.....	sg5	8.01	8.34				
3.0.....	gb1	7.79	8.12				
3.0.....	gb2	5.01	5.20				
4.0.....	ms1	74.56	74.70	74.02	74.62	8.22	9.73
4.0.....	ms2	48.25	48.39	48.04	48.52	4.30	4.34
4.0.....	to1	29.31	29.55	29.35	29.71	3.73	2.35
4.0.....	to2	28.43	29.00	28.00	28.80	3.09	2.45
4.0.....	to3	27.63	28.31	20.05	27.54		2.69
4.0.....	sg1	11.85	12.17	9.58	9.12		
4.0.....	sg2	5.96	6.33	5.99			
4.0.....	sg3	4.16	4.21	8.08			
4.0.....	sg4	3.98	4.01	3.44			
4.0.....	sg5	3.97	4.06	3.87			
4.0.....	gb1	3.81	3.93	3.62			
4.0.....	gb2	2.90	2.91				
5.0.....	ms1	70.61	70.47	70.13	70.42	8.24	9.35
5.0.....	ms2	45.75	45.58	45.49	45.70	4.17	4.09
5.0.....	to1	27.35	27.52	27.27	27.68	3.34	2.06
5.0.....	to2	26.50	26.76	25.96	26.69	4.05	2.10
5.0.....	to3	24.98	25.40	18.16	24.73		2.49
5.0.....	sg1	9.22	9.50	14.68	19.50		
5.0.....	sg2	3.93	4.20	5.94	0.00		
5.0.....	sg3	2.47	2.44	3.92	4.55		
5.0.....	sg4	2.31	2.27				
5.0.....	sg5	2.27	2.24				
5.0.....	gb1	2.14	2.13				
5.0.....	gb2	1.73	1.70				

NOTES.—Col. (1): Mass. Col. (2): Label identifying the phase of evolution. Col. (3): The $l = 0$ large spacing averaged over $n = 5–10$. Col. (4): The $l = 0$ large spacing averaged over $n = 10–20$. Col. (5): The $l = 1$ large spacing averaged over $n = 5–10$. Col. (6): The $l = 1$ large spacing averaged over $n = 10–20$. Col. (7): The $l = 0$ small spacing averaged over $n = 5–10$. Col. (8): The $l = 0$ small spacing averaged over $n = 10–20$. The spacings are in units of μHz.

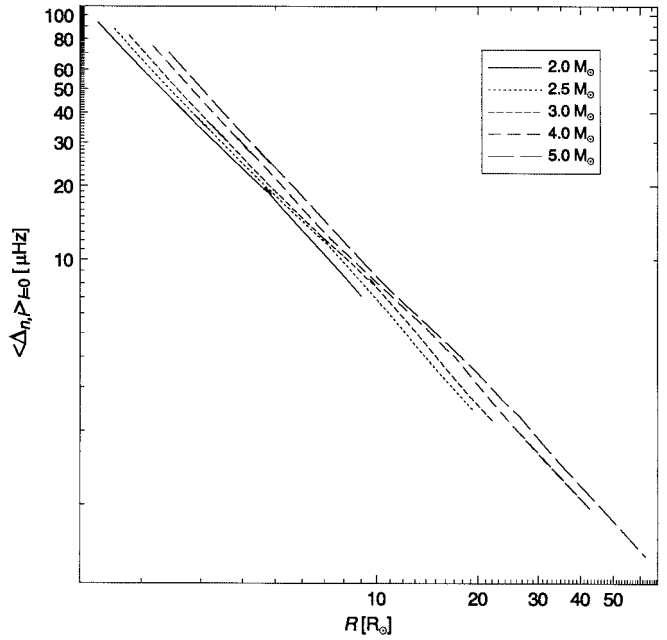

FIG. 29.—Large spacing (see text for definition) averaged over $n = 10$–20 for $l = 0$ p-modes vs. total stellar radius is shown for all of the intermediate-mass stellar models. Curves connect models along their evolutionary track, starting on the ZAMS in the top-left corner and evolving to the base of the giant branch in the bottom-right corner.

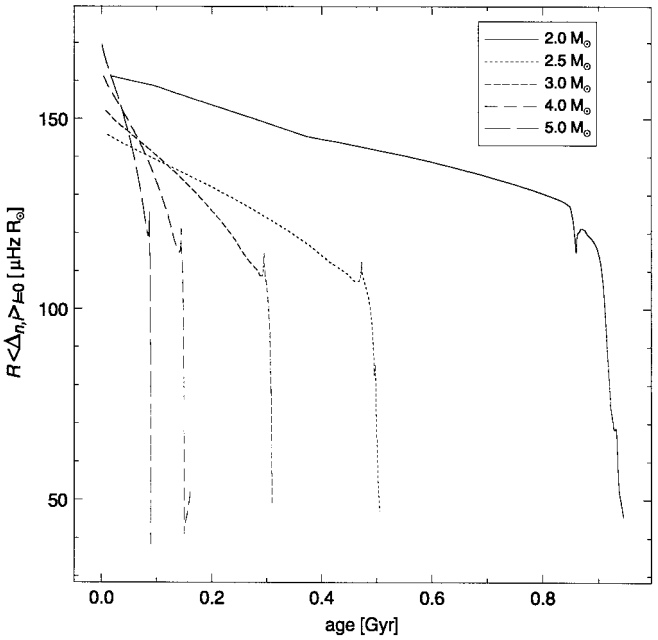

FIG. 31.—Large spacing averaged over $n = 10$–20 for $l = 0$ p-modes times the total stellar radius vs. age is shown for all of the intermediate-mass stellar models.

small spacing will not be useful for these stars during any phase of their evolution.

5.4. *Individual Frequencies*

The frequencies of the $l = 0$ and $l = 1$ oscillation modes from $n = 1$–20 for all of the models pulsed are shown in Figures 35 and 36. The figures show the real component of the frequency versus λ along the left column of plots and the imaginary component of the frequency versus λ along the right column of plots. The time dependence of the oscillation mode goes as $\exp(i\omega t)$, where $\nu = \omega/2\pi$. A negative imaginary component in the frequency corresponds to a mode that is driven; that is, under the assumptions of the model it is expected to be excited. The modes were calculated taking into account nonadiabatic effects associated with radiation, i.e., the kappa mechanism, but do not include the effects of mode coupling to turbulent convective

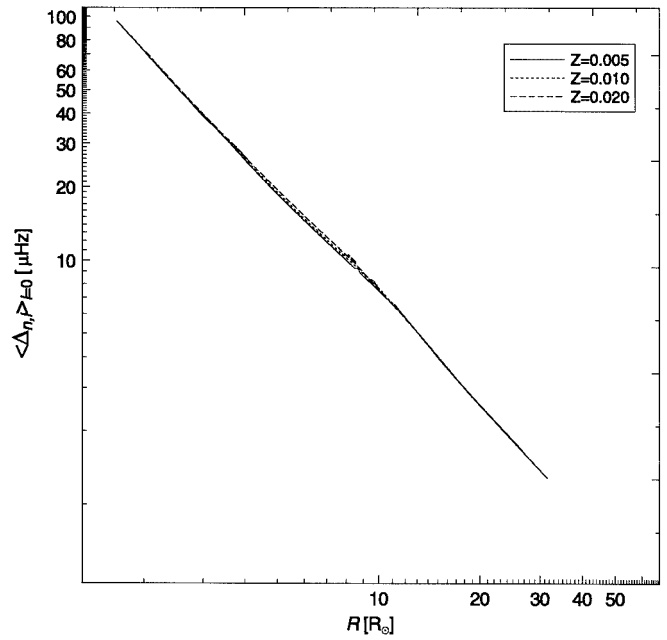

FIG. 30.—Large spacing averaged over $n = 10$–20 for $l = 0$ p-modes vs. total stellar radius is shown for the 3 $M_\odot$ stellar models with different metallicities. The plot shows that the averaged large spacing does not depend significantly on Z.

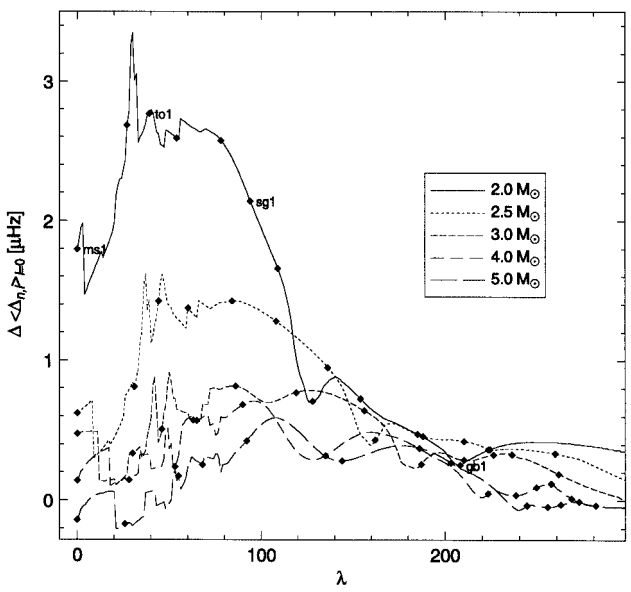

FIG. 32.—Difference between the large spacing averaged over $n = 10$–20 and the large spacing averaged over $n = 5$–10 for $l = 0$ p-modes vs. λ is shown for all the intermediate-mass models. For stars less than 3 $M_\odot$, this difference depends on mass.

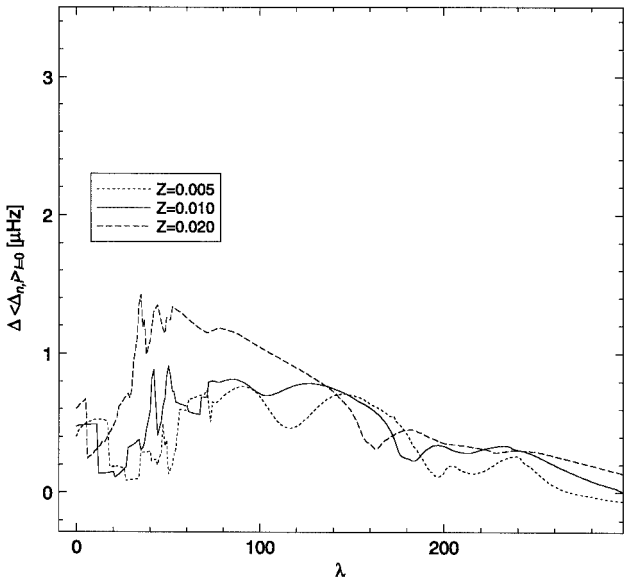

FIG. 33.—Difference between the large spacing averaged over $n = 10$–20 and the large spacing averaged over $n = 5$–10 for $l = 0$ p-modes vs. λ is shown for the 3 $M_{\odot}$ model at different metallicities.

motions. The predictions of mode excitation should, therefore, be taken only within the context of excitation by radiation.

The general trend of the p-mode frequencies (real component) as the models evolve mimics the changing radii of the models. As the model evolves, its radius, in general, increases; hence, the p-mode frequencies decrease (for a given n) and so does the frequency spacing between the modes. More massive stars evolve to larger radii and hence have a more compressed frequency spectrum.

The gap in the evolution of the modes is a numerical artifact. The code first solves the adiabatic equations, then uses the adiabatic solution as an initial guess to solve the nonadiabatic equations. To control convergence, the code forces the nonadiabatic mode frequency to be near the adiabatic frequency. If the nonadiabatic frequency is significantly different from the adiabatic frequency, for example, by more than one-half the frequency spacing, then the code assumes the convergence has failed. This is what is occurring for all the modes in the gaps. In these situations one has to tweak the code for each mode calculated. Owing to the large number of modes calculated, this was not realistically possible. Based on hand-tweaked calculations of a random sample of modes within the gap, it appears that all of the modes in the gap are radiatively excited. This, though, needs to be explored further.

In Figures 37 and 38 we plot all of the models pulsed in an H-R diagram, using large dots to denote those models that are radiatively excited. There is a clear band of models that are radiatively excited that appears on the subgiant branch. The excited models are located redward (*to the right*) of the red edge of the instability strip, within which one finds the classical Cepheids and δ Scuti stars. Note that the models in the gap (where the nonadiabatic calculation failed), which divides the first string of unstable models from the second string of unstable models, are not shown with large dots even though it is likely that they too are all radiatively excited. Examining the work integral associated with the

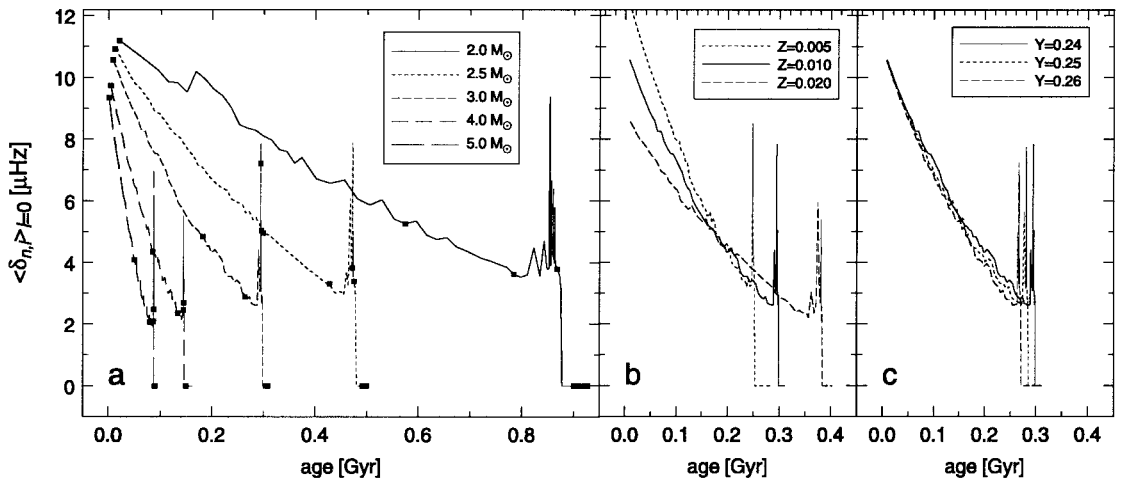

FIG. 34.—(*a*) Small spacing (see text for definition) averaged over $n = 10$–20 for $l = 0$ p-modes vs. age is shown for all of the intermediate-mass stellar models. (*b*) The small spacing averaged over $n = 10$–20 for $l = 0$ p-modes vs. age is shown for the 3 $M_{\odot}$ models with different helium abundances.

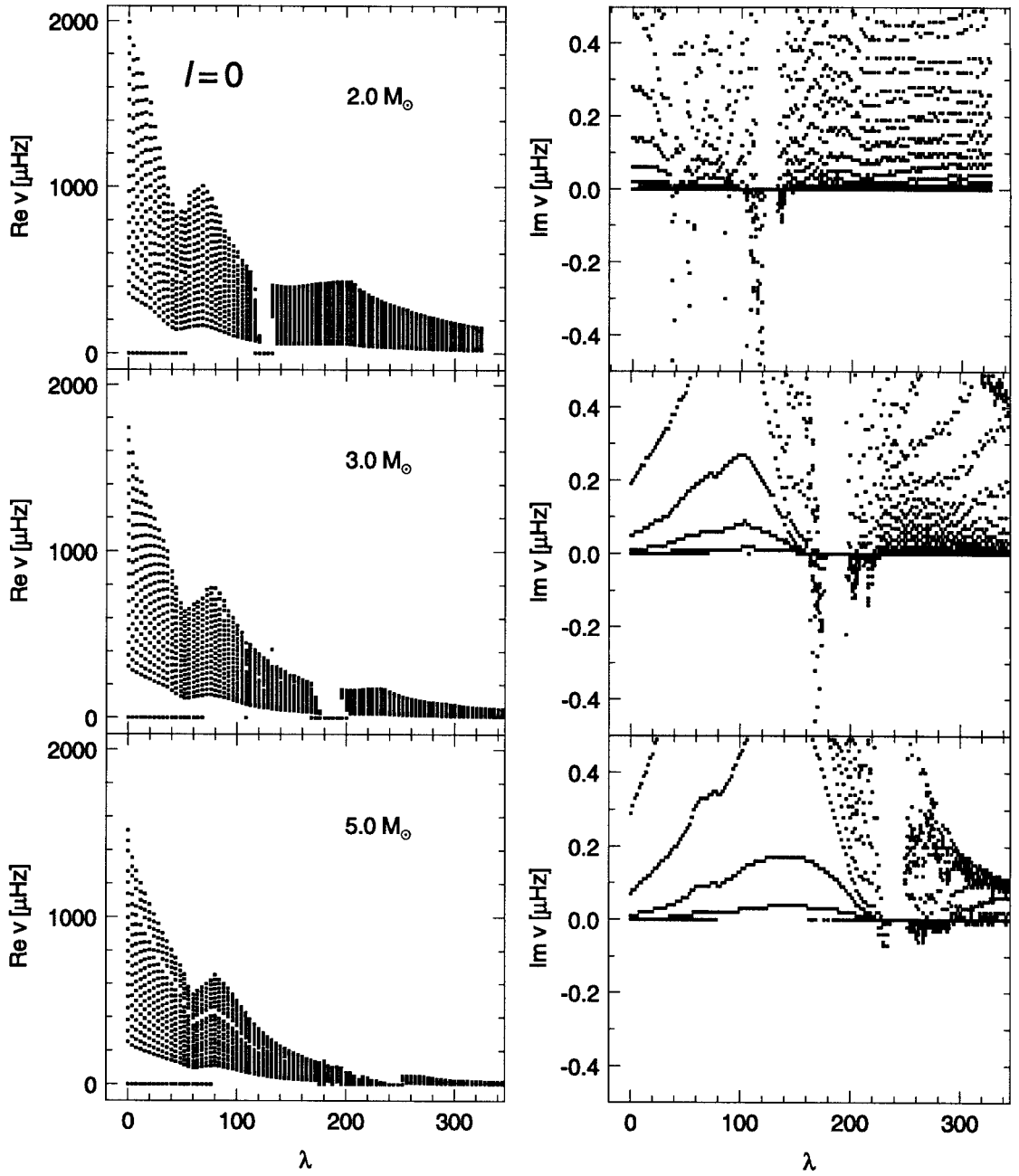

FIG. 35.—Real component of the p-mode frequency (Re ν; *left-hand panels*) and imaginary component of the p-mode frequency (Im ν; *right-hand panels*) for $l = 0$ modes vs. λ are shown for the 2, 3, and 5 $M_\odot$ models. Im ν values below 0 μHz correspond to radiatively excited p-modes.

nonadiabatic modes shows that the largest positive contribution to the work integral occurs just below the surface of the star near the edge of the hydrogen ionization region. In concert, as the star evolves, the surface temperature drops below the ionization temperature of hydrogen, a convective envelope develops, and the star becomes radiatively driven to pulsation. We note that α UMa, for which p-mode oscillations (radial modes only) have been tentatively identified, is a $\sim$4 $M_\odot$ star near the base of the giant branch (Buzasi et al. 2000).

Since g-mode contamination of the p-mode spectrum occurs near the base of the giant branch, $l = 1$ p-mode frequencies are not readily identified in the oscillation spectrum (Guenther et al. 2000) and our calculation of $l = 1$ p-mode frequencies stops short of the giant branch.

5.5. *Mode Bumping*

For more evolved stellar models, when the frequency range of the g-mode spectrum enters the frequency range of the p-mode spectrum, some of the p-modes pick up g-mode–like behavior in the deep interior. First the lower frequency, i.e., lower n-value, p-modes become mixed modes, then as the g-mode spectrum spreads to higher frequencies, so does the presence of mixed modes among the p-modes (Aizenman et al. 1977; Shibahashi & Osaki 1976; Christensen-Dalsgaard 1981; Osaki 1975; Gabriel 1980).

We use the Scuflaire (1974) nomenclature for mode identification that defines the radial order of the mode by $n \equiv n_p - n_g$, where n_p is the number of p-nodes and n_g is the number of g-nodes in the mode. In Table 3 we list the indi-

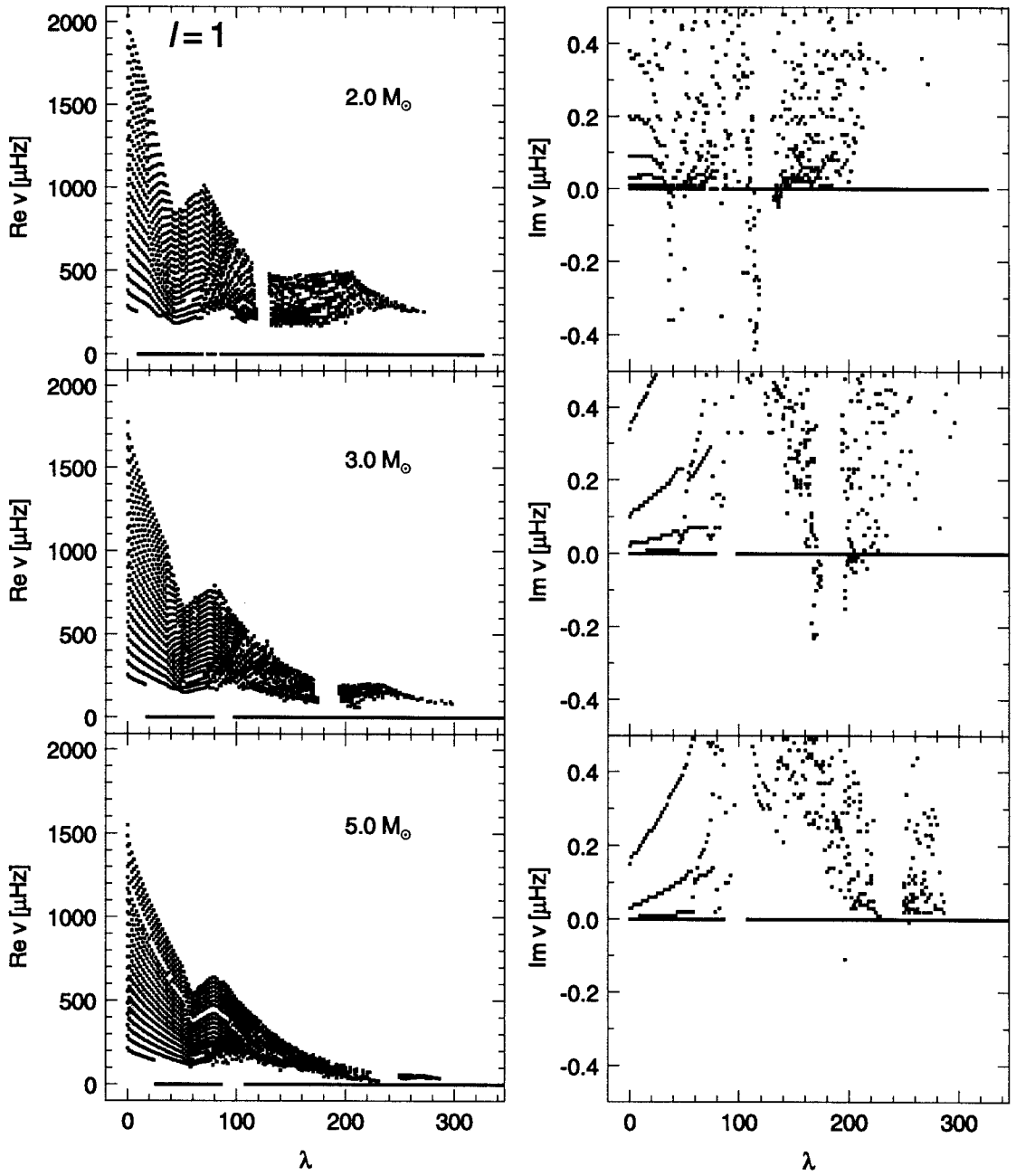

FIG. 36.—Similar to Fig. 35, except $l = 1$ p-mode frequencies are plotted

vidual adiabatic frequencies and mode identifications for the 3 $M_\odot$ model at several stages in the evolution of the model. From the table we can see that the number of g-nodes and the mixing of g-mode–like and p-mode–like behaviors increases as the star evolves.

When the contamination is confined to low–n-value modes, the p-mode frequencies are slightly perturbed. In Figure 39 we plot a small section of Figure 36 to show how the p-mode frequencies are shifted (the wavelike structure) as their frequencies approach and nearly bump into the frequencies of g-modes. Mode bumping, as seen by the ripple in frequencies in Figure 39, moves toward higher frequencies as the model evolves. For a given model, i.e., age, one observes irregular large spacings below the frequency range contaminated by the g-mode spectrum. If this irregular spacing were observed, it would not only confirm the existence of g-modes but also would enable a very precise determination of the evolutionary phase of the star. By the time the star nears the giant branch (see Table 3, model 200, $l = 1$), the contamination by g-modes is such that the nonradial p-mode spectrum is lost in the forest of g-modes.

In Figure 40, we plot the evolution of the adiabatic frequencies for several selected $l = 0$ and $l = 1$ p-modes for the 3 $M_\odot$ models. Each n-value is given a distinct plot symbol. Following the evolution of the $n = 11$, $l = 1$ p-mode frequency, one sees the frequency decrease as the star evolves off of the main sequence ($\lambda = 0$–53), then the mode disappears from $\lambda = 54$ to 64 before reappearing again at $\lambda = 65$. This artifact is a consequence of the radial order nomenclature and mode bumping. In Table 4 we illustrate the effect of mode bumping on the radial order identification. In the first three columns, for models immediately preceding $\lambda = 53$,

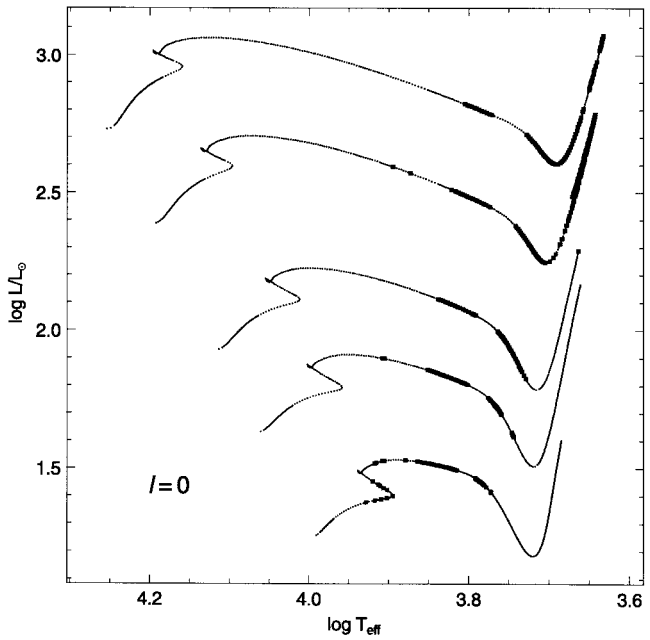

FIG. 37.—H-R diagram of stellar evolutionary tracks of stars of intermediate mass with the models that have radiatively excited $l = 0$ p-modes indicated by large dots.

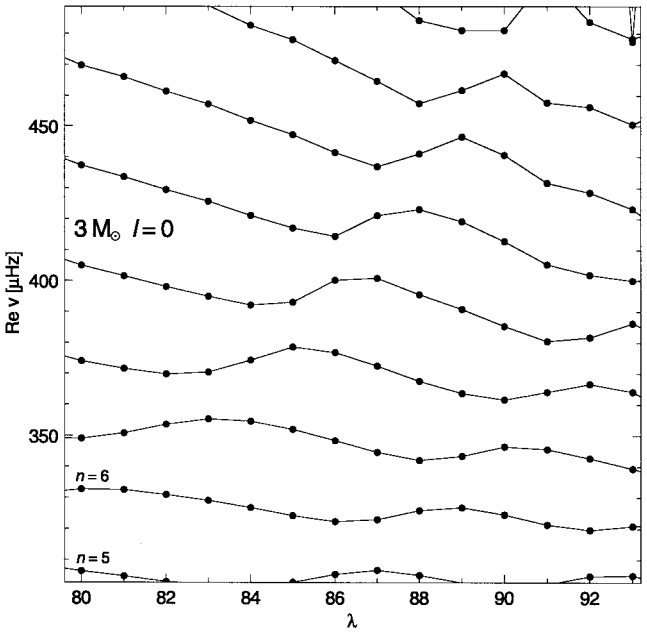

FIG. 39.—Enlarged portion of the 3 $M_\odot$ panel, real component of frequency, in Fig. 35, showing the rippling impression of mode bumping (see discussion in text). The effects of mode bumping propagate to higher frequencies and n-values as the star evolves.

we see that modes up to $n = 11$ are mixed with one g-mode–like node. At the transition to unmixed modes, one n-value is skipped. This is, in part, an artifact of the radial order nomenclature. As the mode mixing advances to higher frequencies and hence higher n-values, the skipped n-value also advances. The situation is even more complicated when the p-mode is mixed with several g-mode–like nodes (see $\lambda = 100$ p-modes in Table 3). Returning to Figure 40, the $n = 11$, $l = 1$ p-mode reappears when, at $\lambda = 65$, the skipped n-value advances beyond this mode. For lower n-value $l = 1$ p-modes, the mixing of g-modes affects not

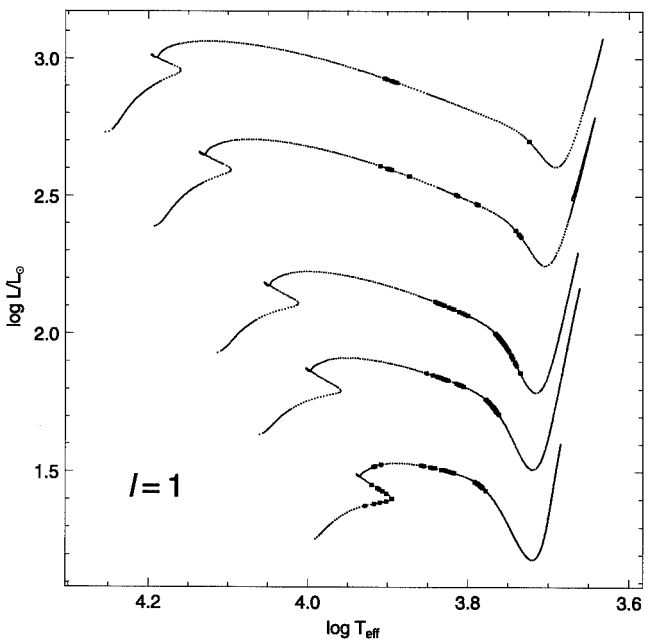

FIG. 38.—H-R diagram of stellar evolutionary tracks of stars of intermediate mass with the models that have radiatively excited $l = 1$ p-modes indicated by large dots.

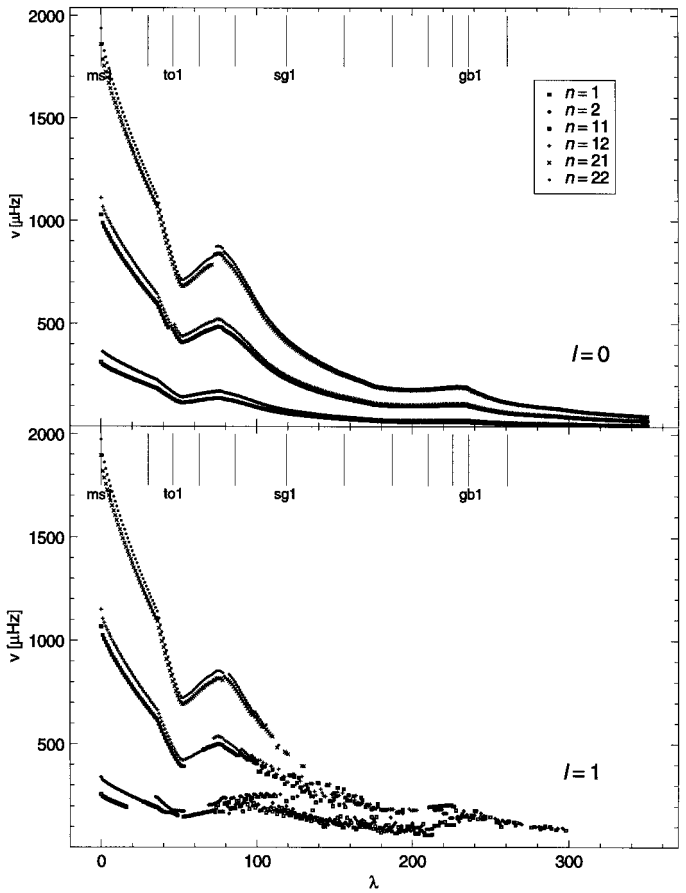

FIG. 40.—Similar to the 3 $M_\odot$ panels, real component of frequency, in Fig. 35 ($l = 0$) and Fig. 36 ($l = 1$), for selected n-values (identified in the legend).

TABLE 3

p-MODES OF SELECTED 3 $M_\odot$ MODELS

$\lambda = 0$					$\lambda = 100$					$\lambda = 200$				
l	n	n_p	n_g	ν	l	n	n_p	n_g	ν	l	n	n_p	n_g	ν
0...	0	0	0	244.5	0	0	0	0	74.0	0	0	0	0	16.5
0...	1	1	0	310.8	0	1	1	0	95.0	0	1	1	0	23.7
0...	3	2	0	376.7	0	2	2	0	118.3	0	2	2	0	31.0
0...	4	3	0	452.7	0	3	3	0	142.0	0	3	3	0	38.2
0...	5	4	0	533.3	0	4	4	0	165.7	0	4	4	0	45.5
0...	6	5	0	615.6	0	5	5	0	188.8	0	5	5	0	53.0
0...	7	6	0	699.4	0	6	6	0	211.9	0	6	6	0	60.7
0...	8	7	0	783.1	0	7	7	0	235.9	0	7	7	0	68.3
0...	9	8	0	866.1	0	8	8	0	260.4	0	8	8	0	75.5
0...	10	9	0	948.0	0	9	9	0	285.4	0	9	9	0	83.0
0...	11	10	0	1029.9	0	10	10	0	310.6	0	10	10	0	90.9
0...	12	11	0	1112.1	0	11	11	0	335.5	0	11	11	0	98.9
0...	13	12	0	1195.1	0	12	12	0	359.8	0	12	12	0	106.8
0...	14	13	0	1278.6	0	13	13	0	383.3	0	13	13	0	114.6
0...	15	14	0	1362.7	0	14	14	0	406.8	0	14	14	0	122.4
0...	16	15	0	1447.0	0	15	15	0	431.2	0	15	15	0	130.3
0...	17	16	0	1531.3	0	16	16	0	456.5	0	16	16	0	138.3
0...	18	17	0	1615.2	0	17	17	0	482.2	0	17	17	0	146.3
0...	19	18	0	1698.1	0	18	18	0	508.0	0	18	18	0	154.4
0...	20	19	0	1779.4	0	19	19	0	533.6	0	19	19	0	162.2
0...	21	20	0	1858.9	0	20	20	0	558.7	0	20	20	0	169.9
0...	22	21	0	1937.3	0	21	21	0	583.7	0	21	21	0	177.1
0...	23	22	0	2016.3	0	22	22	0	608.8	0	22	22	0	183.9
0...	24	23	0	2097.1	0	23	23	0	634.2	0	23	23	0	190.4
0...	25	24	0	2179.5	0	24	24	0	660.0	1	−127	17	144	7.9
1...	−2	0	2	69.8	1	−66	2	68	23.9	1	−85	12	98	10.5
1...	−1	0	1	103.2	1	−53	0	53	32.9	1	−68	5	74	13.1
1...	1	1	0	255.1	1	−43	0	43	41.2	1	−39	1	41	15.8
1...	2	2	0	337.9	1	−35	0	35	50.8	1	−43	2	46	18.5
1...	3	3	0	415.4	1	−30	0	30	59.8	1	−30	2	33	21.0
1...	4	4	0	494.1	1	−25	0	25	70.9	1	−24	1	25	23.6
1...	5	5	0	575.1	1	−21	1	22	80.2	1	−33	3	36	26.4
1...	6	6	0	657.1	1	−19	1	20	88.1	1	−23	5	28	29.1
1...	7	7	0	740.1	1	−17	1	18	97.4	1	−13	3	16	31.4
1...	8	8	0	822.8	1	−15	2	17	103.7	1	−20	5	25	34.3
1...	9	9	0	904.7	1	−13	2	15	117.1	1	−15	3	18	36.9
1...	10	10	0	986.0	1	−4	2	6	121.5	1	−19	5	24	39.4
1...	11	11	0	1067.7	1	−10	3	13	134.3	1	−23	5	28	41.9
1...	12	12	0	1150.0	1	−9	3	12	143.7	1	−17	5	22	45.0
1...	13	13	0	1233.1	1	−8	3	11	146.8	1	−13	4	17	47.1
1...	14	14	0	1316.8	1	−7	4	11	157.0	1	−28	7	35	49.9
1...	15	15	0	1401.1	1	0	4	4	167.8	1	−14	5	19	52.6
1...	16	16	0	1485.4	1	−5	4	9	173.1	1	−7	5	12	54.5
1...	17	17	0	1569.6	1	0	5	5	185.7	1	−25	9	34	57.3
1...	18	18	0	1653.2	1	−3	5	8	194.5	1	−3	6	9	60.6
1...	19	19	0	1735.5	1	2	6	4	205.5	1	−5	8	13	62.1
1...	20	20	0	1815.9	1	−1	6	7	218.0	1	−7	10	17	65.7
1...	21	21	0	1894.8	1	2	7	5	228.4	1	0	7	7	68.5
1...	22	22	0	1973.4	1	1	7	6	243.9	1	−56	8	64	70.4
1...	23	23	0	2053.2	1	4	8	4	255.9	1	−1	8	9	73.6
1...	24	24	0	2134.8	1	3	9	6	271.0	1	−1	9	10	75.7
					1	6	10	4	288.7	1	−14	11	25	79.3
					1	5	10	5	300.9	1	0	9	9	81.7
					1	6	10	4	320.4	1	−10	12	22	84.4
					1	7	11	4	336.8	1	−6	12	18	87.2
					1	10	12	2	351.3	1	0	11	11	89.8
					1	9	13	4	371.6	1	−3	12	15	91.4
					1	10	13	3	391.7	1	−19	12	31	94.7
					1	11	14	3	405.0	1	−1	11	12	97.6
					1	12	15	3	421.3	1	−8	12	20	99.5
					1	13	16	3	444.1	1	−4	12	16	103.1
					1	14	17	3	468.5	1	1	12	11	104.6
					1	15	17	2	492.8	1	−4	12	16	106.6

TABLE 3—*Continued*

$\lambda = 0$					$\lambda = 100$					$\lambda = 200$				
l	n	n_p	n_g	ν	l	n	n_p	n_g	ν	l	n	n_p	n_g	ν
					1	16	18	2	511.0	1	−6	15	21	110.7
					1	17	19	2	523.9	1	3	14	11	112.2
					1	18	20	2	546.4	1	−2	14	16	114.5
					1	19	21	2	570.6	1	2	15	13	118.8
					1	20	22	2	595.1	1	5	17	12	120.7
					1	21	23	2	620.0	1	−6	16	22	123.5
					1	22	24	2	645.1	1	−23	15	38	125.9
										1	4	15	11	127.6
										1	−3	15	18	130.5
										1	5	16	11	135.2
										1	0	16	16	138.2
										1	6	17	11	143.3
										1	−1	17	18	146.6
										1	−14	18	32	149.9
										1	7	18	11	152.0
										1	−4	19	23	155.9
										1	5	19	14	158.5
										1	4	19	15	161.6
										1	−9	20	29	165.5
										1	8	20	12	167.8
										1	10	21	11	174.4
										1	−5	21	26	178.8
										1	12	22	10	181.2
										1	14	24	10	187.9
										1	−1	23	24	192.6
										1	14	24	10	195.0

TABLE 4

SELECTED EVOLUTION OF RADIAL ORDERS FOR 3 $M_\odot$ $l = 1$ p-MODES

$\lambda = \ldots 53$			$\lambda = 54 \ldots 56$			$\lambda = 57 \ldots 64$			$\lambda = 65 \ldots$		
n.....	n_p	n_g	n	n_p	n_g	n	n_p	n_g	n	n_p	n_g
8.....	9	1	8	9	1	8	9	1	8	9	1
9.....	10	1	9	10	1	9	10	1	9	10	1
11...	12	1	10	11	1	10	11	1	10	11	1
12...	12	0	12	12	0	12	13	1	11	12	1
13...	13	0	13	13	0	13	13	0	13	13	0

only the frequencies (see $n = 1$ and 2, $l = 0$ p-modes in Fig. 40) but also the radial order identification.

The nonradial $l = 1$ p-modes disappear as the star evolves toward the giant branch. The mode frequencies are bumped to frequencies above the acoustic cutoff frequency.

6. SUMMARY

We have reviewed the evolution of the structure and pulsation properties of stars between 2 and 5 $M_\odot$ and have provided extensive plots that show both the evolution of the interior structure and the evolution of the p-mode frequencies. We have also highlighted several physical characteristics of the stellar models that can be readily tested with oscillation data.

We have shown how the large frequency spacing can be used to determine the radius of a star, with little sensitivity to composition. This is important not only because it provides a robust way of determining stellar radii but also because it provides a severe test of the stellar convection model upon which the model-predicted stellar radius depends.

We find that the large spacing varies with n differently for stars of different mass. And as a consequence, it may be possible to use the average of the large spacings in different frequency intervals to determine the masses of stars. The method is sensitive to composition and only works for stars less than 3 $M_\odot$.

The stars considered here do not develop convective envelopes until they are on their approach to the giant branch. We, therefore, do not expect to see Sun-like nonradial p-mode oscillations, that is, oscillations driven by turbulent convection, until the stars develop convective envelopes. This makes stars in the 2–5 $M_\odot$ mass range ideal asteroseismology candidates because detecting the existence of the power envelope associated with p-mode oscillations (there is no need to be able to resolve the oscillation spectrum into modes) indirectly confirms the existence of a convective envelope. By identifying the boundary between those stars that have convective envelopes and those that do not, using

asteroseismology, one tests the stellar model physics associated with convection. It is possible, though, that nonradial *p*-mode oscillations can be driven by the kappa mechanism.

Our solutions to the nonadiabatic, nonradial oscillation equations, which follow radiative gains and losses, reveal specific regions in the H-R diagram, redward of the instability strip, where the *p*-mode oscillations are driven by radiation. In particular, we find that the *p*-modes of subgiants with masses greater than 3 $M_{\odot}$ are radiatively driven when the surface temperature of the star drops below 10,000 K and the star develops a convective envelope. In these stars the kappa mechanism operates in the hydrogen ionization region to drive the oscillations. We note, though, that nonadiabatic effects due to turbulent convection are not included in the oscillation calculation and the degree to which this might affect the prediction of oscillation excitation is unknown.

When intermediate-mass stars do develop a convective envelope, their evolution is advanced to the point where the *g*-mode spectrum overlaps the low–*n*-value *p*-mode spectrum. When a *g*-mode frequency nears the frequency of a *p*-mode, the *p*-mode frequency is perturbed or bumped. The *p*-mode itself becomes dual flavored, taking on *g*-mode–like oscillatory behavior in the interior and maintaining *p*-mode–like oscillatory behavior near the surface. The contamination is such that by the time the star reaches the subgiant phase of evolution, the regular spacing between nonradial *p*-modes is completely destroyed. Radial modes are not effected since radial *g*-modes are undefined.

The degree to which the low-frequency *p*-modes are perturbed by mode bumping, that is, how far to higher frequencies the irregular spacing associated with mode bumping has extended, can be used to determine the precise evolutionary phase of a star.

It is a fortuitous coincidence that as stellar structure theory advances with the development of physically realistic models of stellar convection, nonradial *p*-mode oscillation observations will soon become available to test these models. Although it is difficult to predict exactly how far-reaching asteroseismology's impact will be on astrophysics, it is clear, as we have tried to show here for a small population of stars, that asteroseismology will change the way we model stars, even if only to add to the observable constraints.

This work was supported in part by an NSERC grant to the author.

REFERENCES

Ahmad, Q. R., Allen, R. C., & Andersen, T. C. 2001, Phys. Rev. Lett., 87, 071301
Aizenman, M., Smeyers, P., & Weigert, A. 1977, A&A, 58, 41
Alexander, D. R., & Ferguson, J. W. 1994, ApJ, 437, 879
Bahcall, J. N., Pinsonneault, M. H., & Basu, S. 2001, ApJ, 555, 990
Boger, J., et al. (SNO Collaboration). 2000, Nucl. Instrum. Methods Phys. Res. A, 449, 172
Brown, T. M., Gilliland, R. L., Noyes, R. W., & Ramsey, L. W. 1991, ApJ, 368, 599
Buzasi, D., Catanzarite, J., Laher, R., Conrow, T., Shupe, D., Gautier, T. N., III, Kreidl, T., & Everett, D. 2000, ApJ, 532, L133
Chaboyer, B., Sarajedini, A., & Armandroff, T. E. 2000, AJ, 120, 3102
Chandrasekhar, S. 1957, An Introduction to the Study of Stellar Structure (New York: Dover)
Christensen-Dalsgaard, J. 1981, MNRAS, 194, 229
Demarque, P., Guenther, D. B., & Kim, Y.-C. 1999, ApJ, 517, 510
Demarque, P., Zinn, R., Lee, Y.-W., & Yi, S. 2000, AJ, 119, 1398
Deupree, R. G. 2001, ApJ, 552, 268
Fukuda, Y., et al. 1998, Phys. Rev. Lett., 81, 1562
Gabriel, M. 1980, A&A, 82, 8
Grevesse, N., Noels, A., & Sauval, A. J. 1996, in ASP Conf. Ser. 99, Cosmic Abundances, ed. S. S. Holt & G. Sonneborn (San Francisco: ASP), 117
Guenther, D. B. 1994, ApJ, 422, 400
Guenther, D. B., & Demarque, P. 1993, ApJ, 405, 298
———. 1997, ApJ, 484, 937
Guenther, D. B., & Demarque, P. 2000, ApJ, 531, 503
Guenther, D. B., Demarque, P., Buzasi, D., Catanzarite, J., Laher, R., Conrow, T., & Kreidl, T. 2000, ApJ, 530, L45
Guenther, D. B., Demarque, P., Kim, Y. -C., & Pinsonneault, M. H. 1992, ApJ, 387, 372
Iben, I., Jr. 1967, ARA&A, 5, 571
Iben, I., Jr., & Mahaffy, J. 1976, ApJ, 209, L39
Iglesias, C. A., & Rogers, F. J. 1996, ApJ, 464, 943
Kim, Y.-C., & Chan, K. L. 1998, ApJ, 496, L121
Kjeldsen, H., & Bedding, T. R. 1995, A&A, 293, 87
Nordlund, A., & Stein, R. F. 1996, in Stellar Evolution: What Should be Done: Proc. 32nd Liège International Astrophysical Colloquium, ed. A. Noels, D. Fraipont-Caro, M. Gabriel, N. Grevesse, & P. Demarque (Liège: Univ. Liège, Inst. Astrophysique), 75
Osaki, Y. 1975, PASJ, 27, 237
Rogers, F. J. 1986, ApJ, 310, 723
Rogers, F. J., Swenson, F. J., & Iglesias, C. A. 1996, ApJ, 456, 902
Scuflaire, R. 1974, A&A, 36, 107
Shibahashi, H., & Osaki, Y. 1976, PASJ, 28, 199
Sills, A., Faver, J. A., Lombardi, J. C., Jr., Rasio, F. A., & Warren, A. R. 2001, ApJ, 548, 323
Tassoul, M. 1980, ApJS, 43, 469
Unno, W., Osaki, Y., Ando, H., & Shibahashi, H. 1979, Nonradial Oscillations of Stars (Tokyo: Univ. Tokyo Press)